CORE
Metadata, citation and similar papers at core.ac.uk
Provided by DSpace@IZTECH Institutional Repository

INVESTIGATION OF MAGNETIC DEAD LAYER FORMATION AT THE INTERFACES OF SPUTTERED $Ni_{80}Fe_{20}$ THIN FILMS

**A Thesis Submitted to
the Graduate School of Engineering and Sciences of
İzmir Institute of Technology
in Partial Fulfillment of the Requirements for the Degree of**

MASTER OF SCIENCE

in Physics

**by
Hüseyin Serhat ALAGÖZ**

**July 2009
İZMİR**

We approve the thesis of **Hüseyin Serhat ALAGÖZ**

Assist. Prof. Dr. Süleyman TARI
Supervisor

Assoc. Prof. Dr. R. Tuğrul SENGER
Committee Member

Assist. Prof. Dr. Ömer MERMER
Committee Member

15 June, 2009

Prof. Dr. Durmuş Ali DEMİR
Head of the Physics Department

Prof. Dr. Hasan BÖKE
Dean of the Graduate School of
Engineering and Sciences

ACKNOWLEDGEMENTS

I would like to express my sincere gratitude to Assist. Prof. Dr. Süleyman Tari who has been my supervisor since the beginning of my study. He provided me many helpful suggestions, constructive advice and constant encouragement during the master thesis.

I am also grateful to express my satisfactions with doctorate candidate Hüseyin Tokuç for his valuable friendship and assisting me with my experimental work. I would like to thank to Serdal Okur for the X-Ray reflectivity measurements. I also thank to TUBITAK for funding the project ‘‘TBAG-105T109’’ during my thesis. I wish to express my cordial appreciation to Fzt. Hasan Esat Alagöz for his precious contributions of moral support anytime and anywhere. I am also pleased to name Delal Alagöz for her unforgotten helpfulness during my masters’ study.

I am pleased to express my gratefulness to all my friends at the department for their sharing out their joyful times with me during my sleepless nights.

ABSTRACT

INVESTIGATION OF MAGNETIC DEAD LAYER FORMATION AT THE INTERFACES OF SPUTTERED $Ni_{80}Fe_{20}$ THIN FILMS

In this thesis, magnetic dead layer formation at the interfaces of the sputtered $Ni_{80}Fe_{20}$ thin films has been investigated experimentally. Different insulators such as Ta_2O_5, Al_2O_3 and metallic Ta thin films have been deposited as seed and cap layers to determine the MDL formation at the interface of $Ni_{80}Fe_{20}$.

The magnetization of samples has been probed by Vibrating sample magnetometry and X-ray reflectivity measurements have been carried out to investigate the thickness and roughness of the interlayers. Ta films cause the most MDL formation when grown as seed as well as cap layer. It has been observed that the thickness of MDL is strongly temperature dependent. MDL thickness decreases for all trilayers deposited except for $Ta_2O_5/Ni_{80}Fe_{20}/Ta_2O_5$ when they are exposed to 300 ˚C annealing temperature. Further annealing at 500 ˚C causes an interdiffusion between the layers and the thickness of the MDL increases.

According to XRR measurements, the thickness of the inter alloy layers between the $Ni_{80}Fe_{20}$ and its adjacent layers is consistent with the thickness of magnetic dead layer calculated from Liebermann equation. MDL calculations reveal that $SiO_2/Ta/Ni_{80}Fe_{20}/Al_2O_3$ multilayer has the lowest MDL thickness therefore might be a possible candidate to be used in spin valve structures.

ÖZET

SIÇRATILMIS $Ni_{80}Fe_{20}$ İNCE FİLMLERİN ARAYÜZEYLERİNDE MANYETİK ÖLÜ TABAKA OLUŞUMUNUN İNCELENMESİ

Bu tezde, sıçratılmış $Ni_{80}Fe_{20}$ ince filmlerinin arayüzeylerinde manyetik ölü tabaka oluşumu deneysel olarak incelenmiştir. $Ni_{80}Fe_{20}$ arayüzeylerinde (MÖT) oluşumunu saptamak amacıyla Ta_2O_5 ve Al_2O_3 gibi yalıtkanlar ve metalik Ta ince filmler alt ve üst tabaka olarak büyütülmüştür.

Örneklerin manyetizasyonları, titreşimli örnek magnetometresiyle araştırılmış ve arakatmanların kalınlıkları ve pürüzlülükleri XRR ölçümleri uygulanarak incelenmiştir. Ta filmleri üst tabaka olduğu kadar alt tabaka olarakta büyütüldüğünde en çok MÖT oluşmasına neden olur. MÖT kalınlıklarının ileri derecede sıcaklığa bağlı olduğu gözlenmiştir. 300˚C tavlama sıcaklığına maruz bırakıldıklarında $Ta_2O_5/Ni_{80}Fe_{20}/Ta_2O_5$ dışında büyütülmüş diğer tüm çoklu katmanlar için MÖT kalınlıkları azalır. 500˚C ileri tavlama tabakalar arasındaki ara diffüzyona neden olur ve MÖT kalınlığı artar.

XRR ölçümlerine gore, $Ni_{80}Fe_{20}$ ve komşu tabakalarının arasında oluşmuş ara alaşım kalınlıkları, Liebermann denklemi ile hesaplanan manyetik ölü tabaka kalınlıklarıyla uyumludur. MÖT hesaplamaları, $SiO_2/Ta/Ni_{80}Fe_{20}/Al_2O_3$ çoklu katmanının en düşük manyetik ölü tabakasına sahip olduğunu dolayısıyla muhtemelen spin valf yapılarında kullanılabilecek bir aday olabileceğini göstermiştir.

Dedicated to;

My Perfect Family

For their continued support and encouragement

TABLE OF CONTENTS

LIST OF FIGURES ... ix

LIST OF TABLES ... xi

CHAPTER 1. INTRODUCTION ... 1

CHAPTER 2. MAGNETIC DEAD LAYERS ... 8

2.1. Origin of Atomic Moment ... 8

2.1.1. Spin-spin interaction ... 10

2.1.2. Orbit-orbit interaction ... 11

2.1.3. Spin-orbit interaction ... 12

2.2. Ferromagnetism and Superparamagnetism ... 12

2.3. Magnetically dead layers ... 14

CHAPTER 3. EXPERIMENTAL ... 20

3.1. Magnetron Sputtering System ... 20

3.2. Film Growth Processing ... 22

3.2.1. Growth and Deposition Parameters ... 22

3.3. Characterization Methods ... 23

3.3.1. X Ray Reflectivity (XRR) ... 23

3.3.2. Simulating and Fitting Multilayer Structures ... 25

3.3.3. Basic Equations of XRR and EDP at the Interface ... 28

3.3.4. Vibrating Sample Magnetometer (VSM) ... 31

CHAPTER 4. RESULTS AND DISCUSSION 34
4.1. Vibrating Sample Magnetometer (VSM) and MDL Results 34
4.1.1. $SiO_2/Ta/Ni_{80}Fe_{20}/Ta$ 34
4.1.2. $SiO_2/Ta/Ni_{80}Fe_{20}/Ta_2O_5$ 36
4.1.3. $SiO_2/Ta_2O_5/Ni_{80}Fe_{20}/Ta_2O_5$ 38
4.1.4. $SiO_2/Ta/Ni_{80}Fe_{20}/Al_2O_3$ 41
4.1.5. $SiO_2/Al_2O_3/Ni_{80}Fe_{20}/Ta$ 43
4.3. X Ray Reflectivity Measurements Results (XRR) 45
4.3.1. SiO_2/Ta(5nm)/$Ni_{80}Fe_{20}$(7.6nm)/Ta(3nm) 45
4.3.2. SiO_2 /Ta(5nm)/$Ni_{80}Fe_{20}$(7.6nm)/Ta_2O_5(3nm) 47
4.3.3. SiO_2/Ta_2O_5(3nm)/$Ni_{80}Fe_{20}$(7.6nm)/Ta_2O_5(3nm) 48
4.3.4. SiO_2/Al_2O_3(5nm)/$Ni_{80}Fe_{20}$(7.6nm)/Ta(3nm) 50
4.3.5. SiO_2/Ta(5nm)/$Ni_{80}Fe_{20}$(7.6nm)/Al_2O_3(5nm) 53

CHAPTER 5. CONCLUSIONS 55

REFERENCES 57

LIST OF FIGURES

Figure **Page**

Figure 1.1. Schematic of spatial distribution of scattering centers a) AMR and b) GMR. .. 2

Figure 1.2. Schematic representation of giant magnetoresistance (GMR) in spin valves.... 3

Figure 1.3. Schematics of energy band diagram for two ferromagnetic electrodes............ 5

Figure 1.4. Schematic of Magnetic Tunneling Junction in MRAM architecture. 6

Figure 2.1. Schematic view of a) orbiting and b) spinning electron 8

Figure 2.2. Schematic view of orbit-orbit interaction of orbiting electrons. 11

Figure 2.3. Schematic view of spin orbit interaction. 12

Figure 2.4. Schematic view of magnetic alignment under externally applied field........... 12

Figure 2.5. Schematic of a) longitudal and b) perpendicular recording mechanism. 13

Figure 2.6. Dead layer calculation for a number of discrete nickel samples. 14

Figure 2.7. Determination of magnetic dead layers (MDL). 16

Figure 2.8. Evolution of the ferromagnetic phase of ultrathin Fe films. 17

Figure 2.9. In situ MOKE intensity and hysteresis loops for various Fe thicknesses. 18

Figure 2.10. The interdiffusion of two layers of different atoms. 19

Figure 3.1. Schematic view of sputtering process. 21

Figure 3.2. ATC ORION 5 UHV Magnetron Sputtering System. 22

Figure 3.3. Schematics of specular X-ray reflectivity and thin film multilayers. 24

Figure 3.4. X ray reflectivity data of a test sample. 25

Figure 3.5. Software schematics of `Edit Sample` section. 26

Figure 3.6. XRR curves for the a) measured and b) fitted data. 27

Figure 3.7. XRR data for Pt/$BaTiO_3$ layer and EDP profiles shown in the insert. 29

Figure 3.8. Experimental and simulated XRR data of 50 nm NiFe film. 30

Figure 3.9. Hysteresis curve of a Fe film. 31

Figure 3.10. Schematic illustration of vibrating sample magnetometer (VSM). 33

Figure 3.11. Lakeshore 7400 Vibrating Sample Magnetometer (VSM). 33

Figure 4.1. a) Magnetic hysteresis loops of as deposited Ta/$Ni_{80}Fe_{20}$(d)/Ta trilayers and MDL's at b) 300 ˚C and c) 500 ˚C annealing temperatures 35
Figure 4.2. Angle dependence of saturation magnetic moment for the $Ni_{80}Fe_{20}$ film. 36
Figure 4.3. a) Magnetic hysteresis loops of as deposited Ta/$Ni_{80}Fe_{20}$(d)/Ta_2O_5 trilayer and MDL's at b) 300 ˚C and c) 500 ˚C annealing temperatures 37
Figure 4.4. a) Magnetic hysteresis loops of as deposited Ta_2O_5/$Ni_{80}Fe_{20}$(d)/Ta_2O_5 trilayer and MDL's at b) 300 ˚C and c) 500 ˚C annealing temperatures 39
Figure 4.5. XPS measurements Ta/$Ni_{80}Fe_{20}$/Ta_2O_5 and Ta_2O_5/$Ni_{80}Fe_{20}$/Ta_2O_5 trilayers ... 40
Figure 4.6. a) Magnetic hysteresis loops of as deposited Ta/$Ni_{80}Fe_{20}$(d)/Al_2O_3 trilayer and MDL's at b) 300 ˚C and c) 500 ˚C annealing temperatures 41
Figure 4.7. a) XRD patters b) XRR measurements for Ta/$Ni_{80}Fe_{20}$/Al_2O_3 multilayer. 42
Figure 4.8. a) Magnetic hysteresis loops of as deposited Al_2O_3/$Ni_{80}Fe_{20}$(d)/Ta trilayer and MDL's at b) 300 ˚C and c) 500 ˚C annealing temperatures 44
Figure 4.9. XRR measurement of SiO_2/Ta(5nm)/$Ni_{80}Fe_{20}$(7.6nm)/Ta(3nm) layer 45
Figure 4.10. XRR measurement of SiO_2/Ta(5nm)/$Ni_{80}Fe_{20}$(7.6nm)/Ta_2O_5(3nm) layer. 47
Figure 4.11. XRR measurement of SiO_2/Ta_2O_5(3nm)/$Ni_{80}Fe_{20}$(7.6nm)/Ta_2O_5(3nm) layer. 49
Figure 4.12. XRR measurement of SiO_2/Al_2O_3(5nm)/$Ni_{80}Fe_{20}$(7.6nm)/Ta(5nm) layer 51
Figure 4.13. XRR measurement of SiO_2/Ta(5nm)/$Ni_{80}Fe_{20}$(7.6nm)/Al_2O_3(5nm) layer. 53

LIST OF TABLES

Table **Page**

Table 3.1. Layers grown for investigation of magnetic dead layers. 23

Table 4.1. Table of XRD specifications and MDL's of $Ta/Ni_{80}Fe_{20}/Al_2O_3$ multilayer. 43

Table 4.2. Magnetic dead layers of $Ni_{80}Fe_{20}$ for each stack. 44

Table 4.3. Segmented fit model of SiO_2/Ta(5nm)/$Ni_{80}Fe_{20}$(7.6nm)/Ta(3nm). 46

Table 4.4. Segmented fit model of SiO_2/Ta(5nm)/$Ni_{80}Fe_{20}$(7.6nm)/Ta_2O_5(3nm). 48

Table 4.5. Segmented fit model of SiO_2/Ta_2O_5(3nm)/$Ni_{80}Fe_{20}$(7.6nm)/Ta_2O_5(3nm). 50

Table 4.6. Segmented fit model of SiO_2/Al_2O_3(5nm)/$Ni_{80}Fe_{20}$(7.6nm)/Ta(5nm)............... 52

Table 4.7. Segmented fit model of SiO_2/Ta(5nm)/$Ni_{80}Fe_{20}$(7.6 nm)/Al_2O_3(5nm)............. 54

CHAPTER 1

INTRODUCTION

Magnetism is the study of interaction between spins, spins and external field or spins and lattice in different length scales. Spin plays a fundamental role for the electron transport in solid state devices. Considering the spin as an extra degree of freedom for the electron transport increased the expectation to fabricate new type of solid state device. Next generation microelectronics device concepts have taken spin property of electron into account. The spin of electron has endeavored to produce spintronic solid state devices. Magnetic tunnel junctions (MRAM) and read head sensors whose working principle is based on tunneling magnetoresistance (TMR) can be built for data storage technology. Today much research is toward producing faster, denser, cheaper and non volatile solid state devices. Yet reducing the device dimension is a challenge. Optimizations of magnetic devices require good deposition techniques to work efficiently. However this is not quite easy due to well known atomic defects. The performances of multilayer systems such as tunnel junctions depend not only on the interface structure but also the growth kinetics of deposited thin film materials. Number of studies have already been done but further is needed to reach the best experimental conditions to get functional integrated magnetic devices.

An interaction between magnetically ordered systems and light was noted by Michael Faraday in 1846. Faraday theory is based on the rotation of polarization plane of linearly polarized light that goes through the magnetized crystal. Remnant state of the crystal determines the rotation of the plane in absence of a magnetic field. Magnetic effect on electrical conductivity is observed by Lord Kelvin in 1856. Magnetoresistance depends on the orientation of remnant magnetization with respect to the direction of the current. Sir Nevill Mott then defined his two current models for the electrical conductance in 1936.

Mott simply made a connection between magnetism and electrical phenomena. According to Mott theory, the electrical conduction is sustained by spin up and spin down electrons. This concept is later confirmed by Campbell and Fert (Fert, et al. 1968) in their two currents conduction in nickel study by introducing the spin-flip scattering process. Angular dependence of current density $\vec{j}$ with respect to the magnetization $\vec{M}$ is called anisotropic magnetoresistance (AMR). The maximum angular magnetoresistance is defined in Equation 1.1:

$$\frac{\Delta R}{R} = \frac{R(j \parallel M) - R(j \perp M)}{R(j \perp M)} \tag{1.1}$$

Spin orbit interaction is weak with repect to exchange interaction which implies that AMR is a small effect. For instance AMR is found to be less than one percent in Ni-based alloy. Scattering centers are random in AMR and hard to manipulate the spin flip scattering events. However, geometrically stacked heteromagnetic thin film layers ensures to modify the spin dependent scattering effects as it is seen in Figure 1.1.

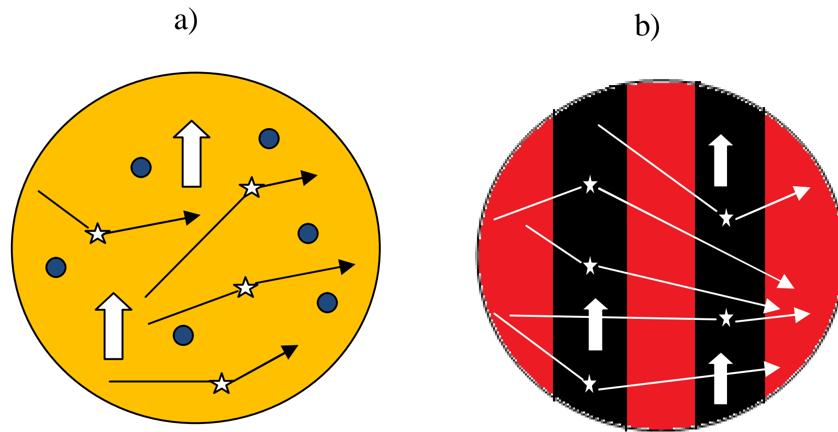

Figure 1.1. Schematic of spatial distribution of scattering centers a) AMR and b) GMR.

For higher storage densities AMR is replaced by giant magnetoresistance (GMR). The thin film magnetism study increased when the growth of magnetic layers could be controlled by molecular beam epitaxy and sputtering deposition technique.

Reducing the thickness to nanometer regime causes emergence of novel quantum effect which affects the magnetic moment and ordering temperature of the material. Fe/Cr multilayers (Baibich, et al. 1988) and Fe/Cr/Fe trilayers (Binasch, et al. 1989) were studied independently by Albert Fert's and P.Grünberg's group. Both studies revealed that a large resistivity change ΔR was observed when the magnetization of the layered stack switched from antiparallel (AP) at zero magnetic field to parallel (P) configuration in an applied field H. Giant magnetoresistance is defined in Equation 1.2:

$$\frac{\Delta R}{R} = \frac{R(H=0) - R(H)}{R(H)} \tag{1.2}$$

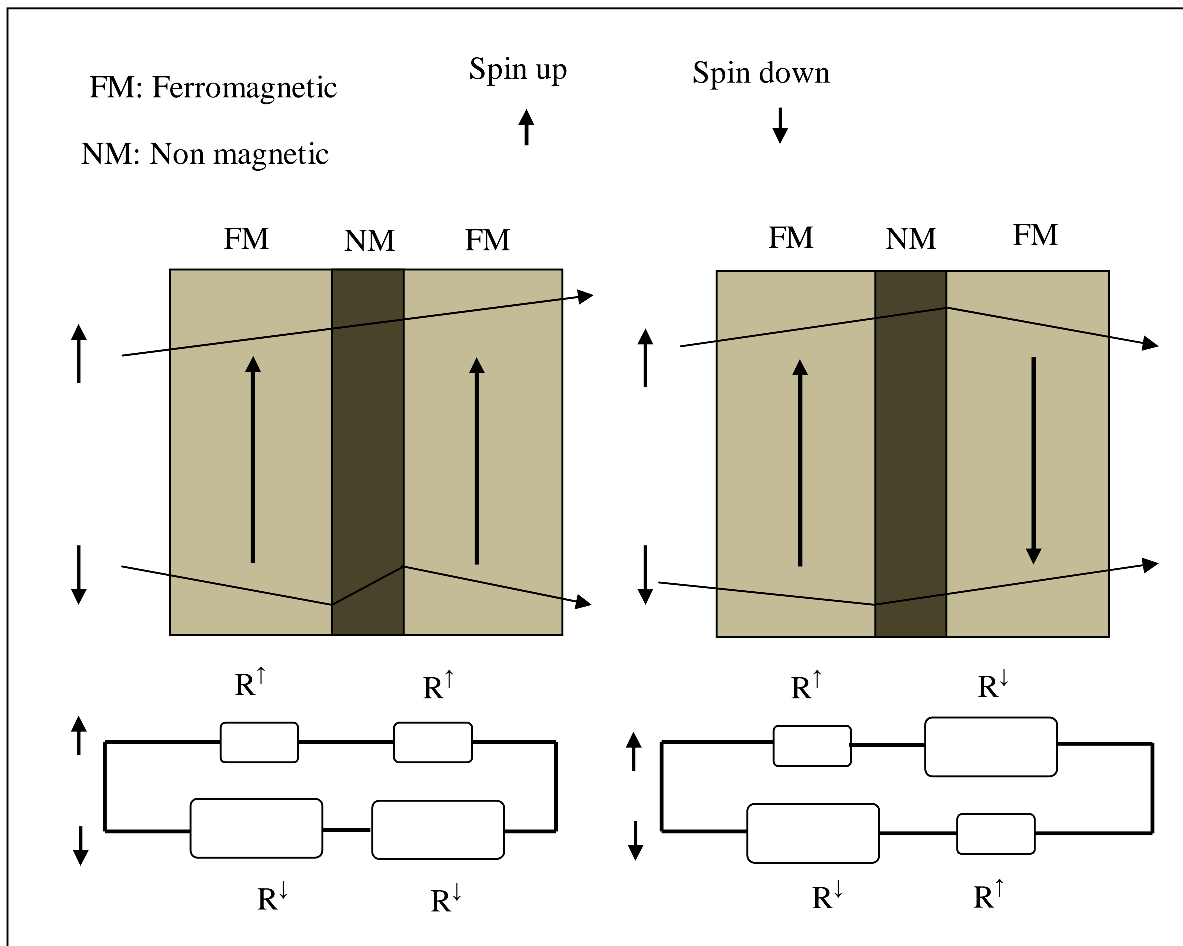

Figure 1.2. Schematic representation of giant magnetoresistance (GMR) in spin valves.

The structure of GMR systems consists of a non magnetic spacer layer between two magnetic layers as shown in Figure 1.2. Giant magnetoresistance can be explained by spin dependent scattering phenomena. When the relative magnetization orientation of two ferromagnetic layers are parallel (P), the spin up electrons pass without scattering yet the spin down electrons scatter in both ferromagnetic electrodes. The resistance increases when the magnetization orientation of two ferromagnetic electrodes is antiparallel (AP). The spin up electrons pass through the first layer but scatters in the second layer, and the spin down electrons scatter in the first layer already. These two scattering events increase the resistance. This abrupt change in the resistance is called giant magnetoresistance (GMR) which is defined in Equation 1.3:

$$G = \frac{R_{\downarrow\uparrow} - R_{\uparrow\uparrow}}{R_{\uparrow\uparrow}} x100 \tag{1.3}$$

The $R_{\uparrow\downarrow}$ and $R_{\uparrow\uparrow}$ represent the resistances when antiparallel and parallel alignment is achieved. GMR ratio depends on several factors. Spacer thickness plays important role due to the fact that it determines the coupling strength between two magnetization states of ferromagnetic electrodes. At very thin spacer, antiparallel alignment can be obstructed due to the interaction between the magnetization vectors.

The main factor is to achieve different states of magnetization alignment. Antiparallel alignment can be obtained by using different coercivities of magnetic layers or by pinning the magnetization using antiferromagnetic material which is directly contacted with ferromagnetic electrode (Ohldag, et al. 2003). The microscopic origin of GMR is due to the density of states of conduction electrons.

The electrons at E_F level contribute the transport phenomena. Then the spin polarization is defined as $P_i = \frac{n_i^{\uparrow} - n_i^{\downarrow}}{n_i^{\uparrow} + n_i^{\downarrow}}$ where $i = L, R$.

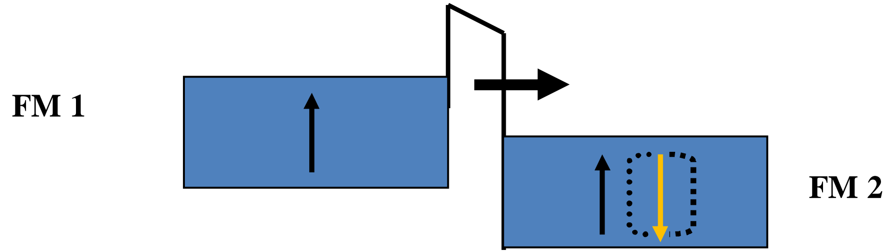

Figure 1.3. Schematics of energy band diagram for two ferromagnetic electrodes.

Where, P_i (i = L, R) are the spin polarizations of conduction electrons in two ferromagnetic electrodes and $n_i^{\uparrow}$, $n_i^{\downarrow}$ are the density of spin up and spin down states at the Fermi level in the i^{th}electrode. Knowing the polarization of conduction electrons in two FM electrodes, one can calculate the GMR ratio. The research of GMR effect shifted to tunneling magnetoresistance (TMR) by introducing thin barrier of insulator instead of a normal metal barrier that separates two magnetic metals.

Electrons can tunnel through the insulator enabling the flow of a current between two magnetic metals when the insulator is sufficiently thin. TMR ratio depends on the resistance changes with respect to relative orientation of magnetization of the magnetic metals, like in GMR effect. Figure 1.3 shows the energy band diagram for the two ferromagnetic electrodes for the TMR based spintronic devices.

The first realization of TMR was obtained by (Julliere, et al. 1975) at very low temperatures. Then (Moodera, et al. 1995), (Miyazaki, et al. 1993) used Al_2O_3 amorphous barrier in magnetic tunnel junction (MTJ) and measured a 100% TMR at room temperature. 1000% TMR ratio is reached by (S. Yuasa et al. 2004) and (S. Parkin et al. 2004) introducing epitaxially grown Fe/MgO/Fe magnetic tunnel junctions.

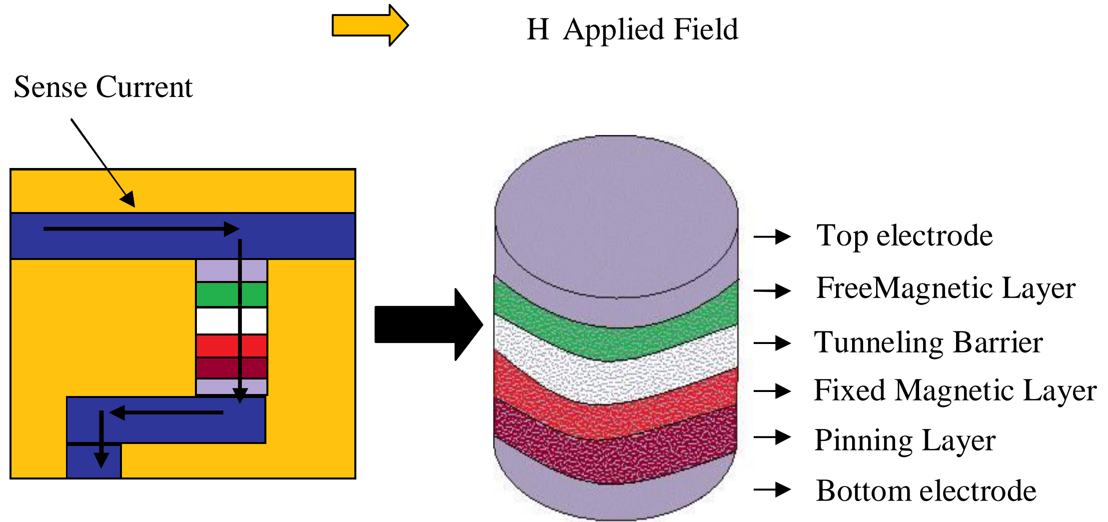

Figure 1.4. Schematic of Magnetic Tunneling Junction in MRAM architecture.

TMR based spintronic devices has a wider range of applications. The most important device is magnetic access memory (MRAM) as shown in Figure 1.4. The information on MRAM is stored in the relative orientation of magnetization of the two ferromagnetic metallic sides of the junction.

Such spin-sensitive devices require well-defined and magnetic interface layers. However, a strong reduction of the magnetization has previously been found for Fe films grown on GaAs. The reduction of the Fe moment was attributed to the magnetically ‘‘dead’’ layers (MDL) near the interface, which would be detrimental to the spin dependent transmission and tunneling between the ferromagnetic metal and the semiconductor substrate (Xu, et al. 1998). Due to high magnetic moment and low magnetostriction, $Ni_{80}Fe_{20}$ is very important among soft magnetic materials (Gong, et al. 2000). Hence, studying $Ni_{80}Fe_{20}$ alloy at the metal-insulator interface is crucial for spintronics device applications.

Determining the roughness of ferromagnetic interface is important for magnetic multilayers exhibiting giant magnetoresistance effect (GMR) (Osgood III, et al. 1999). In this respect, X-ray reflectivity (XRR) measurements are beneficial to use to determine the interface roughness and thickness of multilayers.

In the thesis structural and magnetic properties of $Ta/Ni_{80}Fe_{20}/Ta$, $Ta/Ni_{80}Fe_{20}/Ta_2O_5$, $Ta_2O_5/Ni_{80}Fe_{20}/Ta_2O_5$, $Al_2O_3/Ni_{80}Fe_{20}/Ta$ and $Ta/Ni_{80}Fe_{20}/Al_2O_3$ trilayers were studied. Thickness of magnetically dead layers (MDL) was determined both from magnetization data and X ray reflectivity measurements. Thermally driven interdiffusion is studied at different annealing temperatures (300˚C and 500˚C).

In chapter two, we discuss the principles of magnetism, interface magnetism, formation of magnetic dead layers, temperature effect on MDL and the relation of magnetic dead layers on TMR ratio. In chapter three, we briefly introduce the deposition technique, film growth processing and describe the characterization techniques namely vibrating sample magnetometer (VSM) and X ray reflectivity (XRR). The results and discussions are given in chapter four. The conclusion is given in chapter five.

CHAPTER 2

MAGNETIC DEAD LAYERS

2.1. Origin of Atomic Moment

Magnetism is originated from two types of motions of electrons in atoms-one is the motion of the electrons in an orbit around the nucleus, and the other one is the spin of the electrons around its axis. The spin and the orbital motion independently generate a magnetic moment on each ele ctron causing each of them to behave as a tiny magnet shown in Figure 2.1 (a) and (b).

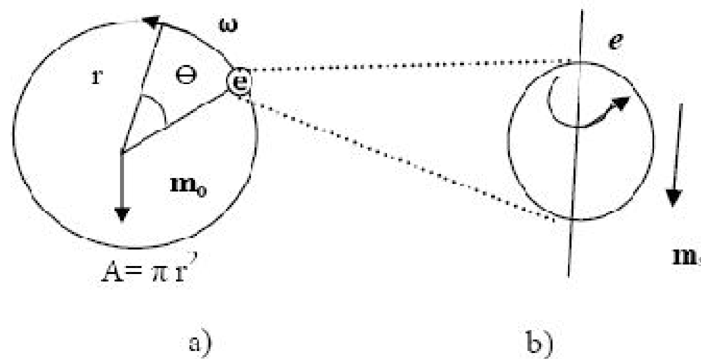

Figure 2.1. Schematic view of a) orbiting electron b) spinning electron.

Magnetic moment of a free electron can be model by considering electron which rounds an atomic nucleus with a radius **r** and angular velocity **ω**. Magnetic moment by orbital motion, $\boldsymbol{\mu_l}$ is defined in Equation 2.1:

$$\mu_l = \mu_0 \mathbf{A}.\boldsymbol{i} \tag{2.1}$$

where, area of the circle is $\mathbf{A} = \pi r^2$ and $\mu_0 = 4\pi . 10^{-7} \left(\frac{\mathrm{H}}{\mathrm{m}}\right)$ is permeability of the vacuum.so one can write the current as fallow in Equation 2.2:

$$\boldsymbol{i} = -\boldsymbol{e}.\boldsymbol{f} = -\boldsymbol{e}\frac{\boldsymbol{\omega}}{\boldsymbol{2\pi}} \text{ current} \tag{2.2}$$

Inserting **A** and $\boldsymbol{i}$ into $\boldsymbol{\mu_l}$, we obtain $A = -\boldsymbol{e}\mu_0\boldsymbol{\omega}\frac{\boldsymbol{r^2}}{\boldsymbol{2}}$. While angular momentum of an electron is given by $\boldsymbol{P_l} = mr^2\boldsymbol{\omega}$ thus magnetic moment of by an electron orbital motion can be expressed as $\mu_l = -(\mu_0\frac{\boldsymbol{e}}{2m})\boldsymbol{P_l}$. According to quantum mechanics, electron orbital motion around an atomic nucleus is quantized so orbital angular momentum is given Equation 2.3: by using the orbital angular momentum number $\boldsymbol{l}$.

$$\boldsymbol{P_l} = \hbar . \boldsymbol{l} \tag{2.3}$$

Thus, magnetic moment due to the orbital motion of an electron is $\mu_l = -\left(\mu_0\frac{\boldsymbol{e}}{2m}\right)\boldsymbol{l} = -\mu_{\mathbf{B}}$ where μ_B is Bohr magneton. From the Dirac equation one can obtain magnetic moment by electron spin that is given by spin angular momentum number **s** given in Equation 2.4:

$$\mu_s = -\left(\mu_0\frac{\boldsymbol{e}}{m}\right)\boldsymbol{P_s} = -\left(\mu_0\frac{\boldsymbol{e}}{m}\right)\hbar . \mathbf{s} = -\mathbf{2}\mu_{\mathrm{B}} . \mathbf{s} \tag{2.4}$$

where $\boldsymbol{P_s} = \hbar . \mathbf{s}$ and $\mathbf{s} = \pm\frac{\mathbf{1}}{\mathbf{2}}$ **.** So total magnetic moment of the electron can be expressed as $\mu = \mu_{\boldsymbol{l}} + \mu_s = -(\boldsymbol{2s} + \boldsymbol{l})\mu_{\mathbf{B}}$ where $\boldsymbol{j} = \boldsymbol{l} + \boldsymbol{s}$ is total angular momentum and this is equal to $-\mathrm{g}\,\mathbf{j}\,\mu_{\mathbf{B}}$ where g is g factor. We can now construct the Hamiltonian (H) of the moving electron by adding the kinetic and the potential energy terms, we have the Equation 2.5:

$$H = \left(\frac{-e^2}{4\pi\varepsilon}\right) x \frac{1}{r^3c^2m^2}\boldsymbol{S}.\boldsymbol{L} \tag{2.5}$$

After correction the H by considering the relativistic factor and the kinematic corrections known as Thomas precession, we have the new Hamiltonian as given in Equation 2.6:

$$H = \left(\frac{-e^2}{8\pi\varepsilon}\right) x \frac{1}{r^3 c^2 m^2} \boldsymbol{S}.\boldsymbol{L} \qquad (2.6)$$

This equation is considered as spin orbit interaction. The physical meaning of this equation is the torque exerted on magnetic dipole moment of the spinning electron. In quantum mechanics the Hamiltonian no longer commutes with L and S. The spin and orbital angular momentum are not separately conserved.

2.1.1. Spin-spin interaction

The effect of the spin-spin interaction can be understood by considering two electrons that the state in which their spins are parallel (S=1, triplet state) will be lower in energy than the state in which their spins are antiparallel (S=0, singlet state). This result is correlated with the fact that the two electrons are identical fermions, and a wavefunction which describes the pair must be antisymmetric with respect to exchange of the electrons (Pauli Exclusion Principle). Then the wavefunction can be considered to be the product of the space and spin wavefunctions as given in Equation 2.7:

$$\Psi_{2e}(\text{antisymetric}) = \Psi_{spin}(\text{symetric}) \times \Psi_{space}(\text{asymetric}) \qquad (2.7)$$

The fact that the spins are parallel makes the spin part of the wavefunction symmetric, and forces the space part to be antisymmetric. An anti-symmetric space wavefunction for the two electrons implies a larger average distance between them than a symmetric function of the same type. The probability is the square of the wavefunction,

and from a simple functional point of view, the square of an antisymmetric function must go to zero at the origin. So in general, the probability for small separations of the two electrons is smaller than for a symmetric space wavefunction. If the electrons are on the average further apart, then there will be less shielding from the nucleus by the other electron, and a given electron will therefore be more exposed to the nucleus. This implies that it will be more tightly bound and of lower energy.

2.1.2. Orbit-orbit interaction

If two electrons in an atom spend a lot of time close to each other, then they contribute a repulsive or positive potential energy, implying that their energy level will be higher. If the electrons are orbiting in the same direction (and so have a large total angular momentum) they meet less often than when they orbit in opposite directions.

Hence their repulsion is less on average when L is large. The fact that such electron configurations have lower energy means that they will be filled first. Two states can be seen in Figure 2.2.

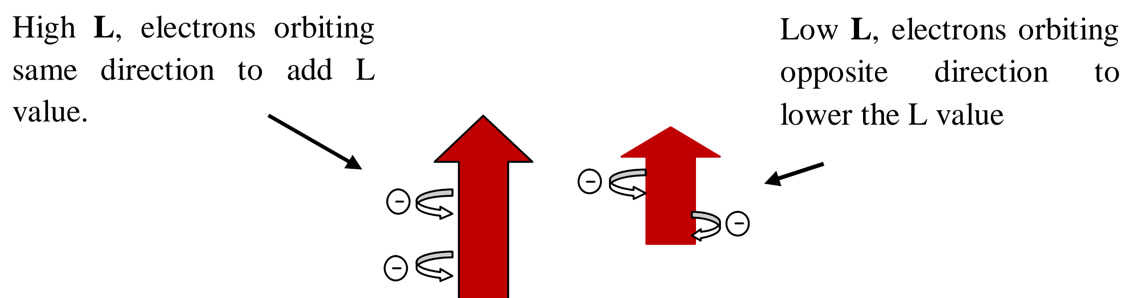

Figure 2.2. Schematic view of orbit-orbit interaction of orbiting electrons.

2.1.3. Spin-orbit interaction

The energy levels of atomic electrons are affected by the interaction between the electron spin magnetic moment and the orbital angular momentum of the electron. It can be visualized as a magnetic field caused by the electron's orbital motion interacting with the spin magnetic moment. This effective magnetic field can be expressed in terms of the electron orbital angular momentum. The interaction energy is that of a magnetic dipole in a magnetic field as shown in Figure 2.3. then the interaction energy can be written as $E = \vec{\mu} \cdot \vec{\boldsymbol{B}}$ where μ comes from electron spin and B comes from orbital motion.

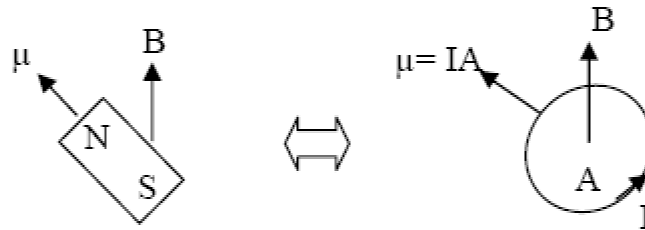

Figure 2.3. Schematic view of spin orbit interaction.

2.2. Ferromagnetism and Superparamagnetism

In some materials especially, those with only atoms with partially filled shells (unpaired spins) can experience a net magnetic moment in the absence of an external field. Ferromagnetic materials contain many atoms with unpaired spins. When these tiny magnetic dipole moments are aligned in the same direction, they create a measurable macroscopic field that is shown in Figure 2.4.

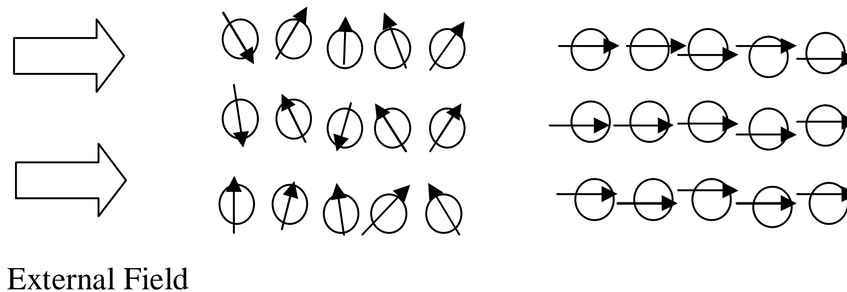

External Field

Figure 2.4. Schematic view of magnetic alignment under externally applied field.

When the temperature increases, thermal motion competes with the ferromagnetic tendency for dipoles to align. When the temperature rises beyond a critical point, called Curie temperature, there is a second-order phase transition and the system can no longer maintain a spontaneous magnetization. The Curie temperature itself is a critical point, where the magnetic susceptibility is theoretically infinite and, although there is no net magnetization, domain-like spin correlations fluctuate at all length scales.

Superparamagnetism is a phenomenon by which magnetic materials may exhibit a behavior similar to paramagnetic even when at temperatures below the Curie or the Neel temperature. This is a small length-scale phenomenon, where the energy required to change the direction of the magnetic moment of the particle is comparable to the ambient thermal energy. At this point, the rate at which the particles will randomly reverse direction becomes significant.

The main challenge in designing magnetic information storage media is to retain the magnetization of the medium despite thermal fluctuations caused by the superparamagnetic limit. At very thin film material shows superparamagnetic behavior and magnetization vector inside the material can be aligned out of the plane and this ensures to pack more data within the recording layer shown in Figure 2.5.(b) (Hitachi Global Storage Technologies).

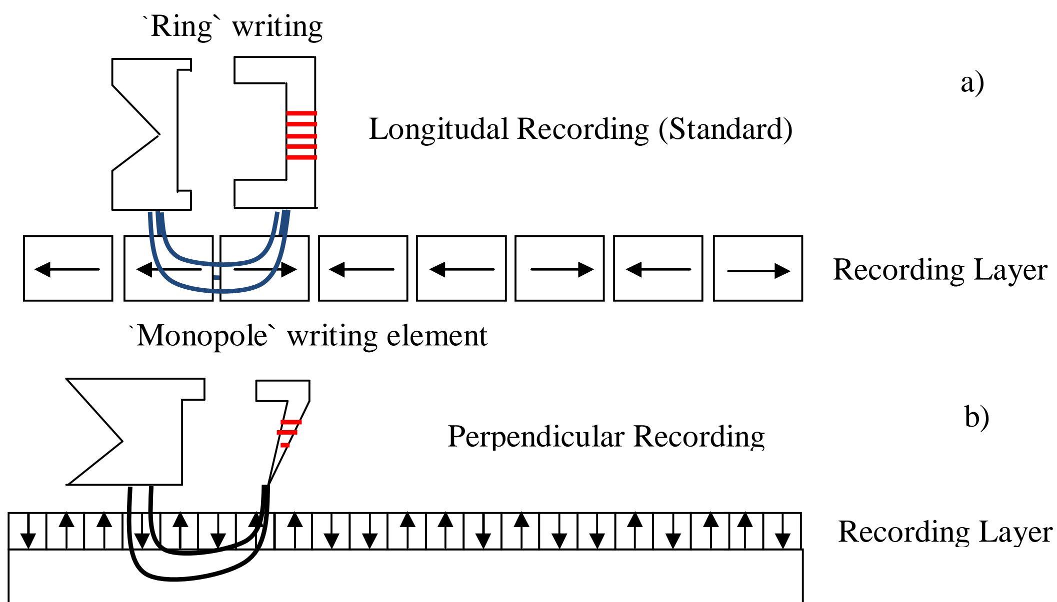

Figure 2.5. Schematic of a) longitudal and b) perpendicular recording mechanism.

2.3. Magnetically dead layers

The magnetic dead layers may form during deposition processes in the order of a few monolayers due to interface diffusion which causes magnetic moment loss of FM electrode. Magnetic dead layer formation and its thickness depend on the temperature, ferromagnetic layer and the layers used to make interfaces with the FM layer. Annealing decreases the MDL thickness for the CoFeB layer (Wang, et al. 2006) but increases for the $Ni_{80}Fe_{20}$ layer (Kowalewski, et al 2000).

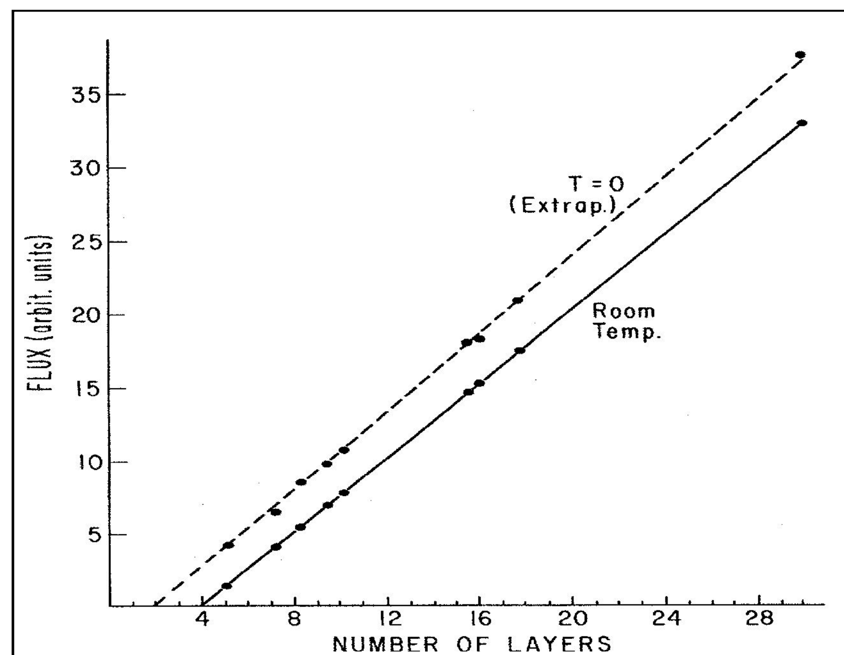

Figure 2.6. Dead layer calculation for a number of discrete nickel samples

Magnetically 'dead' layers on oligatomic (single crystal films of a few atomic layers) films of Fe, Co, Ni were introduced by (Liebermann, et al. 1975). Liebermann investigated the variation of magnetic dead layers of Ni sample by introducing different temperatures. Figure 2.6. shows that there are two and four dead layers at T=0 K and at room temperature respectively.

The magnetic moment m can be written as in Equation 2.7 and Equation 2.8:

$$m = \mu_B \,(D - D_{dead}) \tag{2.8}$$

$$D_{dead} = \frac{Ak_B T}{2\pi C N^2} ln \frac{k_B T}{gH\mu_B} \tag{2.9}$$

The dead layers of Ni at 0 K is attributed to transfer of electrons from s orbital to d orbital in the neighborhood of the surface that means electrons fill the d orbital which decreases the ferromagnetism of the Ni film. Hybridization is also important factor effecting dead layer phenomena. For instance, the magnetic state of Ni/Pt interfaces is quite different from the bulk one due to the changed electronic structure. It has been predicted that not only a band narrowing and increased density-of-state at the Fermi energy at surface and interface in reduced dimension systems, such as thin films and multilayers, increase magnetic moments, but also a strong hybridization of 3*d* electrons between Ni and Cu decreases spin moment. We therefore attribute the observed nonmagnetic layers of Ni at Ni/Pt interfaces to the possible Ni 3*d*–Pt 5*d* hybridization. This leads to a significant reduction in the exchange splitting as a consequence of the balance between the Ni 3*d* majority- and minority-spin densities.

Different thickness of ferromagnetic films like Ni when they are deposited as a seed layer for specific Pd and Pt layers also effects the non magnetic layer formation at the interface, strongly indicates the existence of interfacial effects in Ni/Pt and Ni/Pd multilayers (Jeong, et al. 1999). It could be conjectured that the magnetic moment of Ni adjacent to Pt is suppressed due to an overlapping between the d band of Ni and the conduction band of Pt (Tersoff, et al. 1982). The enhanced magnetic moment in Ni/Pd multilayers might be ascribed to the polarization of the Pd sub-layer (Flevaris, et al. 1991). Thus, the magnetic moment of Ni is strongly dependent the other constituent layer. The detailed band structure of the layer should be known to predict whether the layer yields either suppression or enhancement effect on the magnetization of Ni-based multilayers.

The determination of the magnetic dead layer is simply plotting the saturation magnetic moment with respect to ferromagnetic thickness of the film. Obtained data were fitted by considering errors. If the fitting line passes through the origin then it is said to be there is no magnetic dead layers associated with that FM layer shown in Figure 2.7. Otherwise it passes a certain film thickness (x axis) and the intercept reveals the total magnetic dead layer associated with the two interface of the ferromagnetic film.

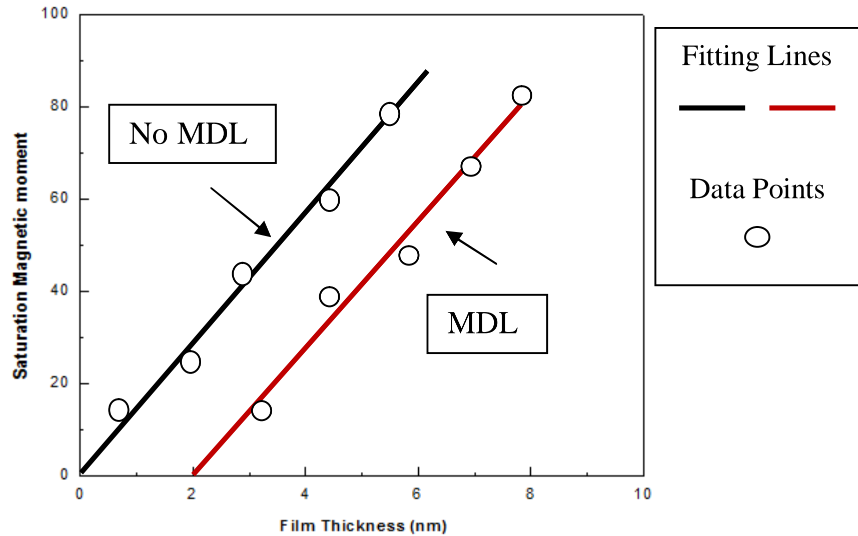

Figure 2.7. Determination of magnetic dead layers (MDL).

Evolution of FM phase of thin films during deposition is an important factor to understand the formation of non magnetic layers exist at interfaces. The evolution of magnetic phases of Fe films on GaAs at room temperature has been modeled by (Xu, et al. 1998). Magnetic ordering of Fe film is shown schematically in the Figure 2.8.

Examining hysteresis loops of Fe with different thickness gives an idea about the evolution of the films. The lack of magnetic signal for the first 3.5 ML for the Fe thin film is due to small cluster size of Fe which is not thick enough to construct a magnetic ordering. The magnetic signal comes from the thick Fe sample that shows good magnetic ordering. Thin Fe layer behaves as superparamagnetic and then non magnetic signals comes out due to irregular ordering of magnetic moment in the sample.

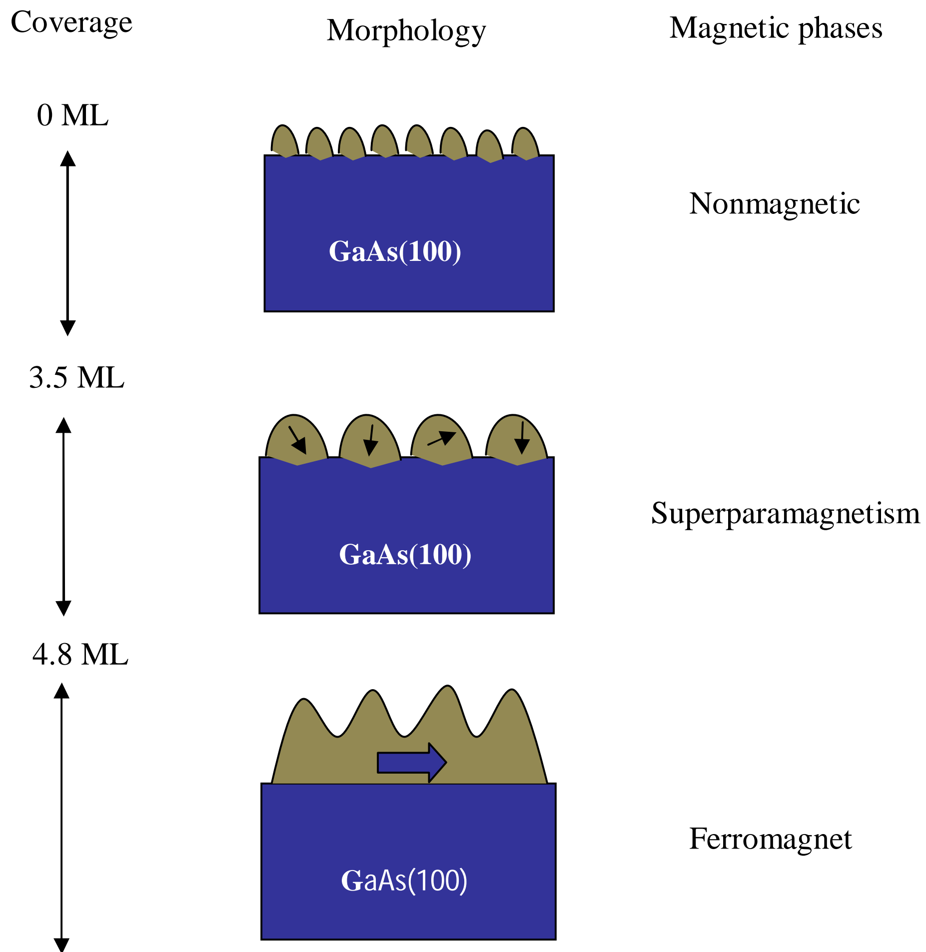

Figure 2.8. Evolution of the ferromagnetic phase of ultrathin Fe films.

Mössbauer method is a very valuable technique for probing the local magnetization in the surface atomic layer, and so determine of dead layers, for the magnetic hyperfine field at some nucleus is essentially proportional to the magnetic moment of its own electron cloud, with only minor contributions from neighboring atoms. (Shinjo, et al. 1992) deposited 1/10 monolayer of Co on top of an electrodeposited thick film of natural Co. They found the same hyperfine field as in the bulk, dead layers are absent. The thickness of non magnetic layers so called dead layer can be estimated in Figure 2.9.

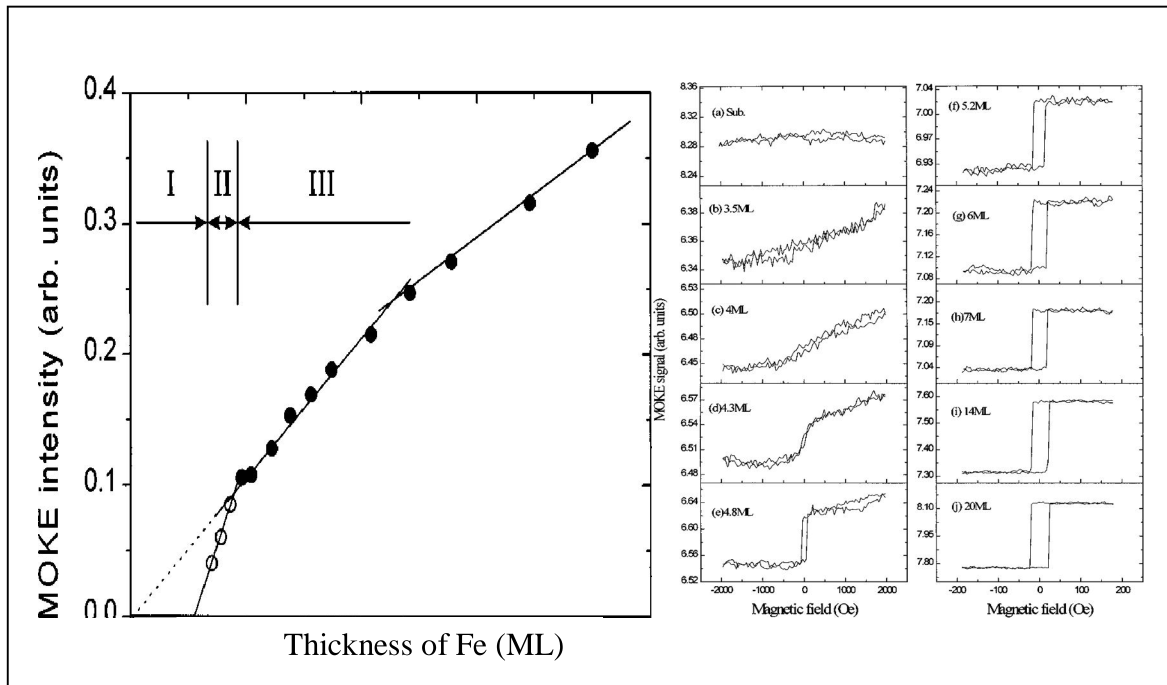

Figure 2.9. In situ MOKE intensity and hysteresis loops for various Fe thicknesses.

The interaction of the low energy electrons with magnetized surfaces may only be used with great care as a tool, to probe the magnetic properties of the very surface layer. For the information depth, if at all known, seems to be several atomic layers in most cases. An indication of dead layers on EuO was given by measurements with polarized electrons (Sattler, et al. 1975). The only electron method which seems to be strictly specific for the first surface layer is electron captures by deuterons. This method records spontaneous magnetization in single crystal Ni surfaces and therefore contradicts the existence of magnetic dead layers.

Figure 2.10. shows interdiffusion of two different atoms during deposition. During deposition incoming atoms with high kinetic energy create interdiffusion (Qiana, et al. 1998) and plays dominant role for reducing magnetic moment of ferromagnets in magnetic tunnel junctions and reducing the spin polarization of electrodes. MDLs are then form due to this interaction between those atoms. Ferromagnetic material’s d orbitals share electrons with adjacent electrons of atoms then not shared electron in the d orbital is reduced. Thickness of the MDLs in general increases in annealing treatments.

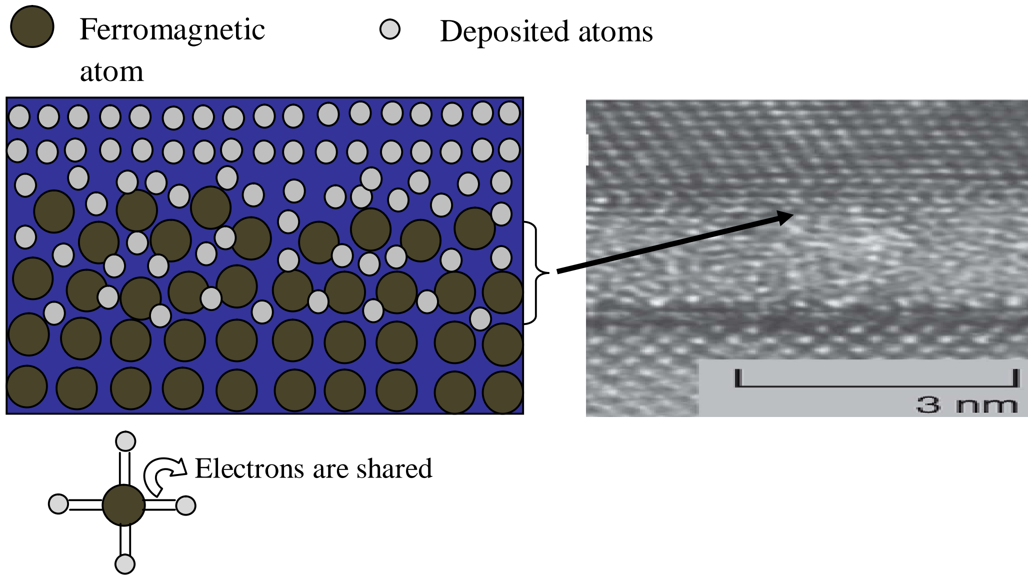

Figure 2.10. The interdiffusion of two layers of different atoms.

CHAPTER 3

EXPERIMENTAL

This chapter covers the experimental methods used in this work to grow and characterize the layers in detail. We used magnetron sputtering system for growing thin films. Magnetic properties of the samples were studied by vibrating sample magnetometer (VSM). X ray reflectivity (XRR) was used to study the interface roughness, densities and the thickness of the samples. The thickness of magnetic dead layers (MDL) of each trilayers was studied with the commonly used Liebermann equation. Thermally driven interdiffusion was studied at 300 ˚C and 500 ˚C annealing temperatures in vacuum.

3.1. Magnetron Sputtering System

Magnetron sputtering is a cheap deposition technique comparing to chemical vapor deposition (CVD) and molecular beam epitaxy (MBE). Since the deposition is well controlled, various materials such as metals or alloys, insulators can be deposited easily.

The principle of magnetron sputtering relies on the momentum transfer of an ionized argon gas that hits the target atom by transferring its kinetic energy to the ejected or sputtered atoms. Then sputtered atom is deposited on a substrate which is located a few cm away from the target. The electron is trapped in the helical motion (magnetic field lines) that is schematically showed in Figure 3.1. The electron encounters the Ar atom that causes the ionization. The heavy Ar ion then hits the target material and removes the target atom.

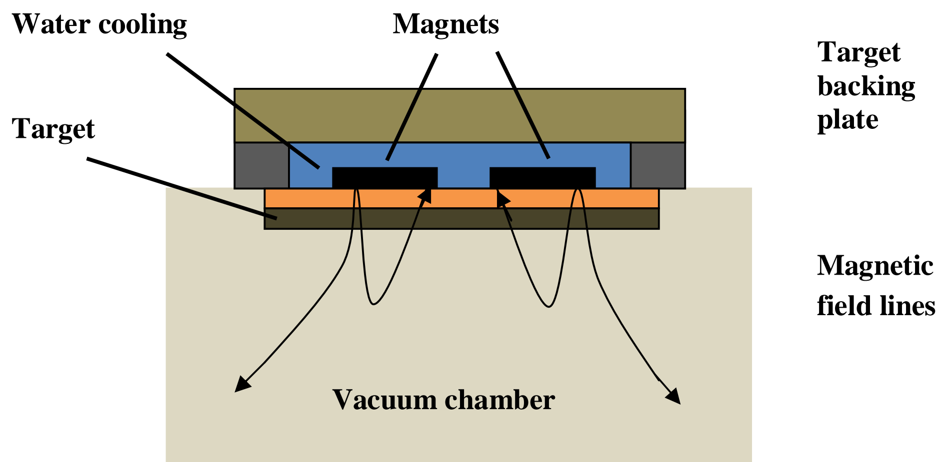

Figure 3.1. Schematic view of sputtering process.

In this thesis, we used an UHV magnetron sputtering system shown in Figure 3.2. to deposit our trilayers of films. The system reaches to 1.7 x10^{-7} torr base pressure in about 20 minutes and consist of two rf and three dc supplies, a maxtek TM-350 thickness monitor, rotating substrate holder that ensures for excellent uniformity and co deposition of alloy films and substrate holder that can be heated up to 850 ˚C.

In general, we use Ar gas for usual deposition and for reactive sputtering we use both O_2 and Ar gases mixture. N_2 gas is used to clean samples before loading into load luck. The system is baked for approximately one day to reach the low base pressure. The targets are presputtered for five minutes before growth process.

Figure 3.2. ATC ORION 5 UHV Magnetron Sputtering System.

3.2. Film Growth Processing

All the films were deposited on one sided polished 500-550 μm thickness of n type <100> Si/SiO_2 based wafers at ambient temperatures. The films were cut by nearly 0.5x0.5 cm^2 area by diamond cutter and measured by caliper with the precision of ± 0.05 cm for VSM measurements. Deposited films were labeled 'magnetic dead layer' with specified film identification number as MDL-001, MDL-002 …and so on.

3.2.1. Growth and Deposition Parameters

Plasma is achieved by applying 240W radio frequency (RF sputtering) power for Al_2O_3 and 45W for reactively sputtered TaO_x. In Dc sputtering, 20W was applied to Ta and $Ni_{80}Fe_{20}$. Thickness was calibrated using MAXTEK thickness monitor given in Table 3.1.

All of the samples were deposited at 3m Torr by letting 10 sccm Ar gas at the throttle position of the valve. Reactive sputtering is performed for Ta_2O_5 insulator by oxidizing the Ta film by introducing mixture of (1/9) Ar-O_2 gases at 45W. Thickness was also confirmed by using atomic force microscopy (AFM).

Table 3.1. Layers grown for investigation of magnetic dead layers.

STRUCTURES
$SiO_2/Ta(5)/Ni_{80}Fe_{20}(d)/Ta(3)$
$SiO_2/Ta(5)/Ni_{80}Fe_{20}(d)/Ta_2O_5(3)$
$SiO_2/Ta_2O_5(3)/Ni_{80}Fe_{20}(d)/Ta_2O_5(3)$
$SiO_2/Ta(5)/Ni_{80}Fe_{20}(d)/Al_2O_3(5)$
$SiO_2/Al_2O_3(5)/Ni_{80}Fe_{20}(10)/Ta(5)$

( ) parenthesis shows the deposition time in minute, **(d)** is 15.2-7.6-3.8-3.04-2.28 and 1.52 nm thickness of $Ni_{80}Fe_{20}$ films.

3.3. Characterization Methods

3.3.1. X Ray Reflectivity (XRR)

X ray reflectivity is a non destructive technique and has become a valuable tool to characterize the interface, thickness, density and roughness of multilayers. X rays are reflected from the interfaces and surface of the films due to different distribution of electron densities in various layers of the thin films. XRR can be used in amorphous, crystalline and liquid samples and generally used for typical layers 5Å-400 nm and interface, surface roughness of 0 to 20 Å.

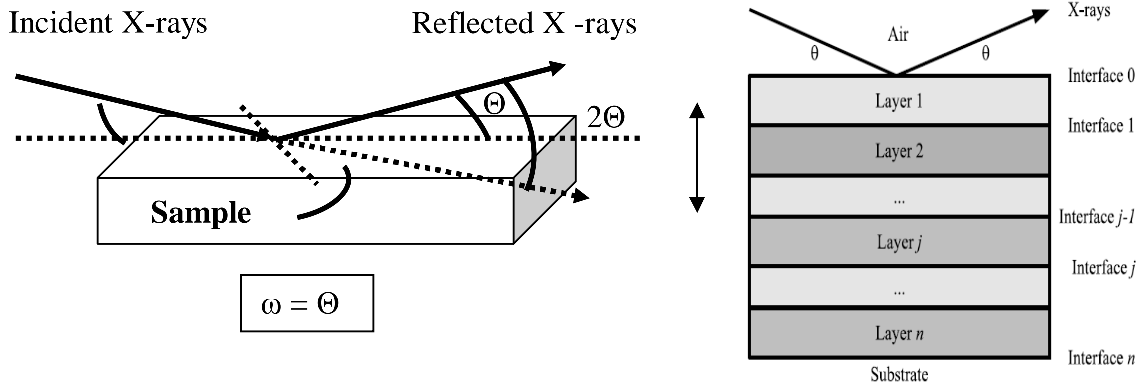

Figure 3.3. Schematics of specular X-ray reflectivity and thin film multilayers.

The Fresnel reflectivity law states that increasing the angle of incidence causes reduction of intensity leaving smooth surface. The detector that receives the intensity coming from the surface requires 5-6 orders of magnitude of intensity and low noise to obtain better fringes coming from the samples. Reducing error during the experiment is quite important thus some alignments such as ω, χ and z scan is needed to eliminate the unwanted signals come from the surface to the detector.

When the angle of incoming X ray is equal to reflected angle, the specular reflectivity condition is reached which is shown with multilayers in Figure 3.3. In the measured data Kiessing fringes shows the thickness of the layer and roughness is determined from the period of those fringes. The variation of electron density profile can be determined from the reflectivity data and the interactions of layers at the interfaces can be obtained due to this electron difference.

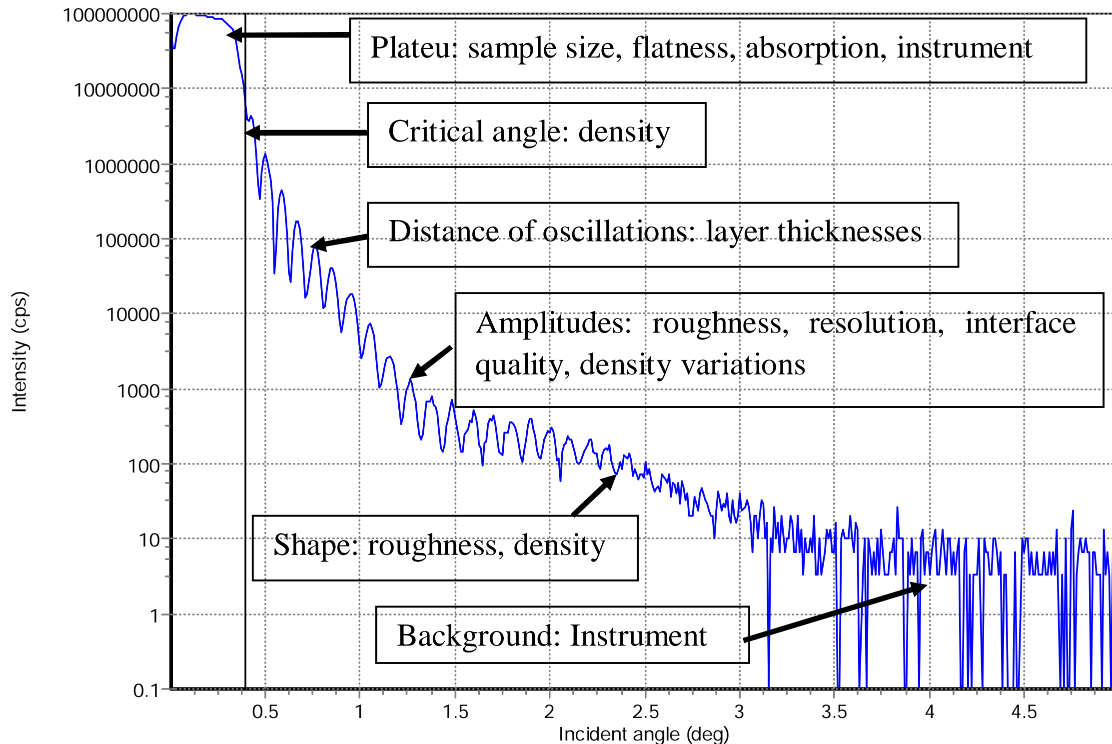

Figure 3.4. X ray reflectivity data of a test sample.

The critical angle is determined when the first periodic fringe appears in the reflectivity curve shown in Figure 3.4. This angle is quite important for the calculation of electron density profiles (EDP) of the interfaces of multilayers. The close oscillated peaks spacing is due to the thickness of each film, the decreasing intensity shows the presence of roughness at the interface or on the surface. In XRR data in general for rougher surfaces the intensity drops due to less reflection and much more absorption. Decay in amplitude is due to interfacial roughness of multilayers.

3.3.2. Simulating and Fitting Multilayer Structures

Before getting started to fit the measured XRR data, first thing to do is to create model by clicking the X`Pert Reflectivity software and choosing the `Edit Sample` icon shown in Figure 3.5. In the Edit Sample section, one can create several layers by choosing structures from `Materials` frame and assigning numbers for thickness, roughness and

densities of each stacks. When all the layers were assigned, pressing the `Set Layer` button, saves the fitting model in `open sample` folder.

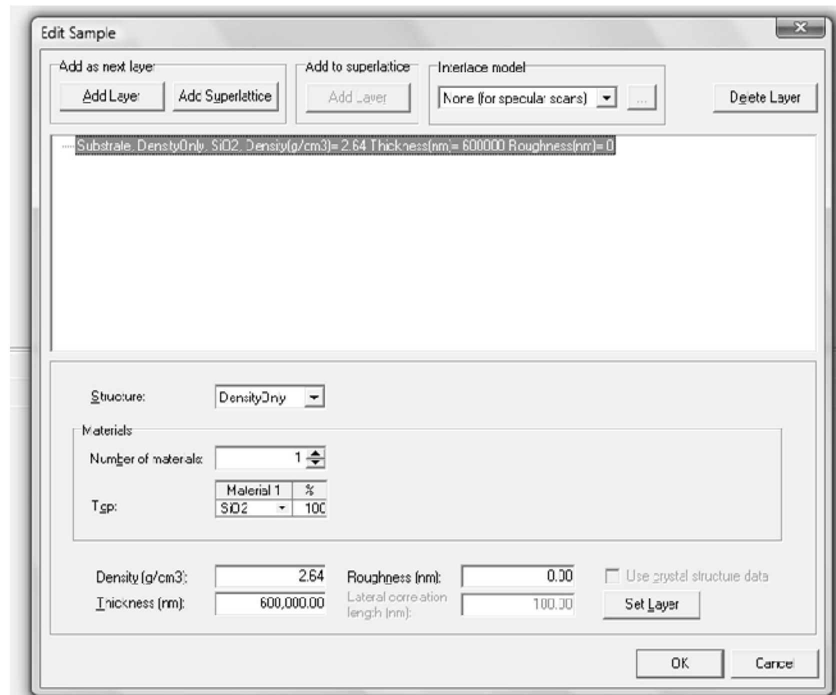

Figure 3.5. Software schematics of `Edit Sample` section.

After editing the sample, the measured XRR file is opened from the `Sample` button. Then `Simulation` button is chosen to setup some parameters such as simulation type and simulation details. Simulation is then generated by clicking `simulate` button. Once simulation is generated, the next step is to open the segmented fit button from fitting section shown in Figure 3.6.a.

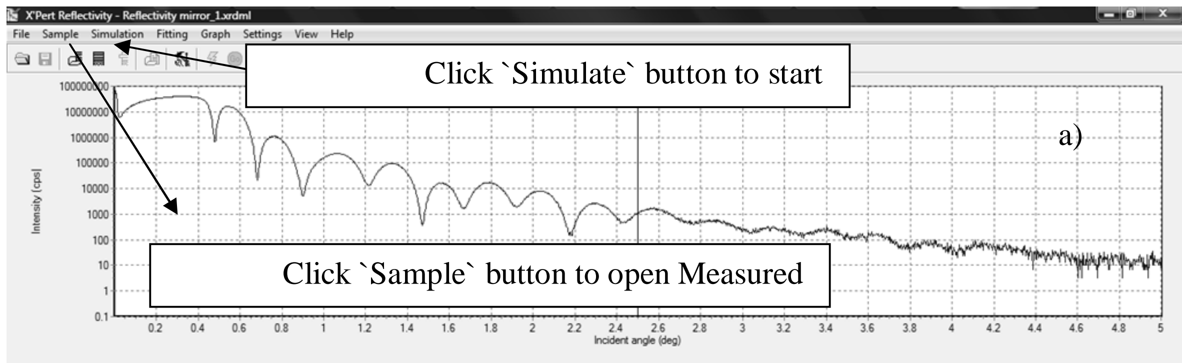

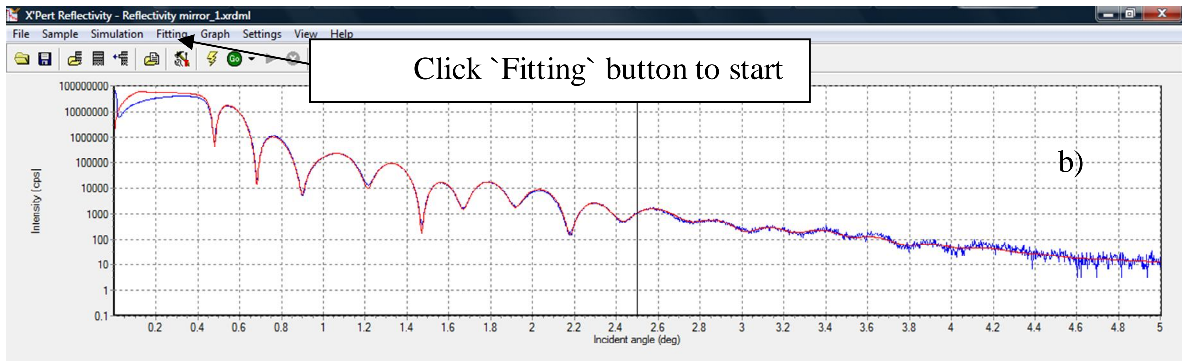

Figure 3.6. XRR curves for the a) measured and b) fitted data.

In the `segmented fit` section thickness and roughness parameters of each layers are changed in order to get best fit. Oxidation should be considered in the `Edit Sample` section in order to get good fits for the measured XRR data.

3.3.3. Basic Equations of XRR and EDP at the Interface

In this section, some principle equations of X-ray reflectivity for ideally flat surfaces are derived by the reference of A.Gibaud and S.Hazra's "X-ray reflectivity and diffuse scattering" study. The interaction of X rays with matter begins with introducing index of refraction which changes the direction of the X ray. The index of refraction of X ray is written as Equation 3.1:

$$n = 1 - \zeta - i\beta \tag{3.1}$$

where ζ and β are related to electron density ρ and linear absorption coefficient μ given in the following Equation 3.2:

$$\zeta = \frac{r_e}{2\pi} \lambda 2 \, \rho \text{ and } \beta = \frac{\lambda}{4\pi} \mu \tag{3.2}$$

where r_e is the classical radius of the electron given as (2.813×10^{-6} nm) and λ is the line radiation of X ray (CuKa-1.5406 Å). Total external reflection of X ray occurs when the incident angle is smaller than the critical angle Θ_c defined in Equation 3.3:

$$\cos \Theta_c = n = 1 - \zeta \tag{3.3}$$

and in the small approximation Taylor expansion yields $\Theta_c{}^2 = 2\zeta = \frac{r_e}{\pi} \lambda^2 \rho$. After giving these relations, the reflected intensity from ideally flat surface will be quite helpful to understand specular reflection. Specular reflection occurs when the incident and the reflected angles at the normal is equal. The specular reflectivity is defined as the ratio of intensity of given angle divided by incoming intensity of the beam as in Equation 3.4:

$$R(\Theta) = \frac{I(\Theta)}{I_O} \tag{3.4}$$

Reflected amplitude is written in the presence of continuity of electric and magnetic field at the interface. The intensity can be described as the critical angle and absorption coefficient of the material given in the Equation 3.5:

$$R^{\text{flat}}(\Theta) = \left|\frac{\Theta-\sqrt{\Theta^2-\Theta_c{}^2-2i\beta}}{\Theta+\sqrt{\Theta^2-\Theta_c{}^2-2i\beta}}\right|^2 \tag{3.5}$$

and more importantly the relation of reflected of an intensity from the surface in a relation of wave vector define as $q_z = \frac{4\pi}{\lambda}\sin\theta$ given as the Equation 3.6:

$$R^{\text{flat}}(q_z) = \left|\frac{q_z-\sqrt{q_z{}^2-q_c{}^2-\frac{32i\pi^2\beta}{\lambda^2}}}{q_z+\sqrt{q_z{}^2-q_c{}^2-\frac{32i\pi^2\beta}{\lambda^2}}}\right|^2 \tag{3.6}$$

Electron density profile (EDP) is quite vital for the determination of interface of the multilayers which gives an evidence of magnetic dead layer.

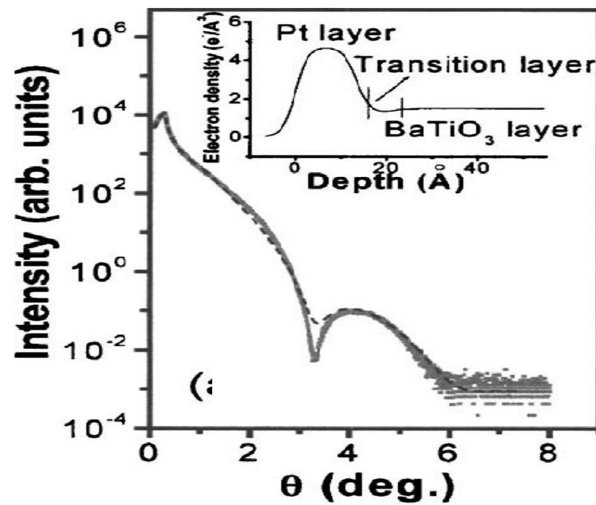

Figure 3.7. XRR data for Pt/$BaTiO_3$ layer and EDP profiles shown in the insert.

EDP is obtained from the simulation data (Li, et al. 2005) shown in the insert of Figure 3.7. From the EDP, one can see that there are three regions: the Pt layer, $BaTiO_3$ layer and the transition layer. This transition layer shows the dead layer at the interface of the Pt/$BaTiO_3$. There is a close relationship between thickness determination from XRR fitting and the magnetic dead layer thickness determination from magnetization data.

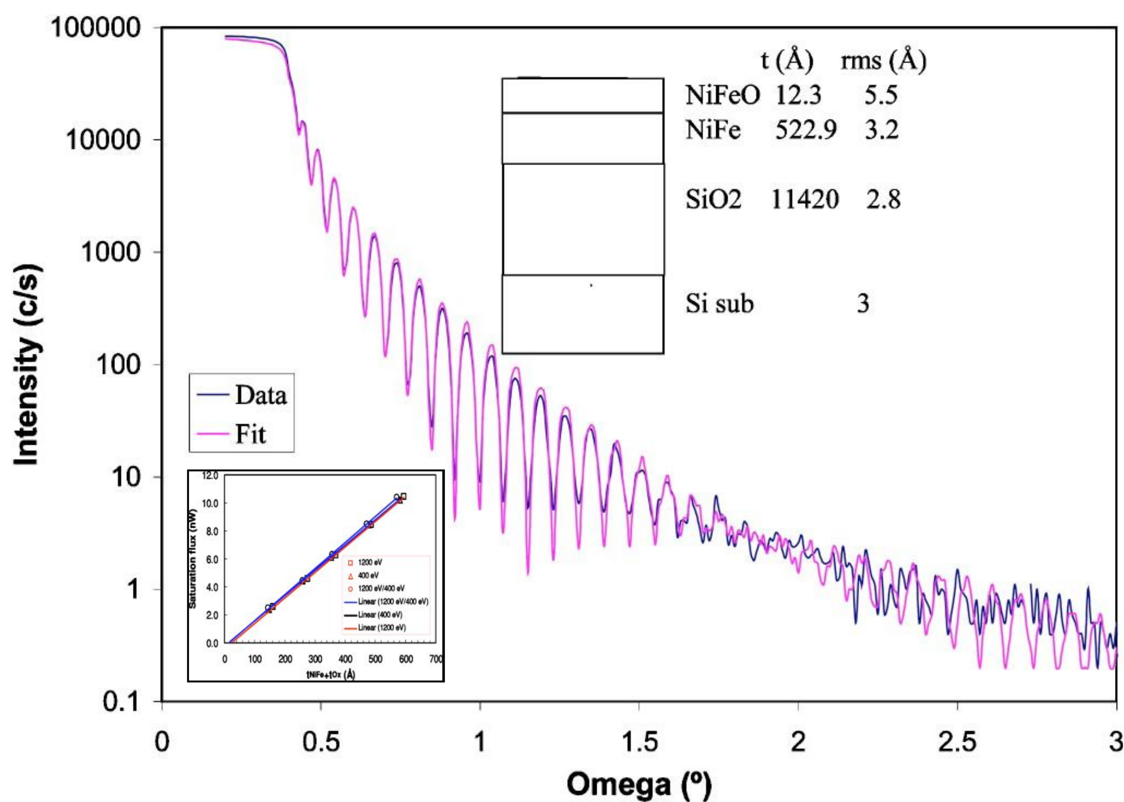

Figure 3.8. Experimental and simulated XRR data of 50 nm NiFe film.

The non magnetic layer formation on top of NiFe film was studied by (Si, et al. 2005) shown in Figure 3.8. According to fit model of reflectivity data of NiFe film, there is 12.3 Å NiFeO layer which has 5.5 Å rms roughness. The 12.3 Å NiFeO layer is attributed as a magnetically dead layer which is also confirmed from magnetization measurements shown in the insert of Figure 3.8.

.

3.3.4. Vibrating Sample Magnetometer (VSM)

Vibrating sample magnetometer has been used widely for determining magnetic properties of materials. A great deal of information can be learned about the magnetic properties of a material by studying its hysteresis loop. A hysteresis loop shows the relationship between the induced magnetic flux density (B) and the magnetizing force (H). It is often referred to as the B-H loop. An example hysteresis loop is shown in Figure 3.9.

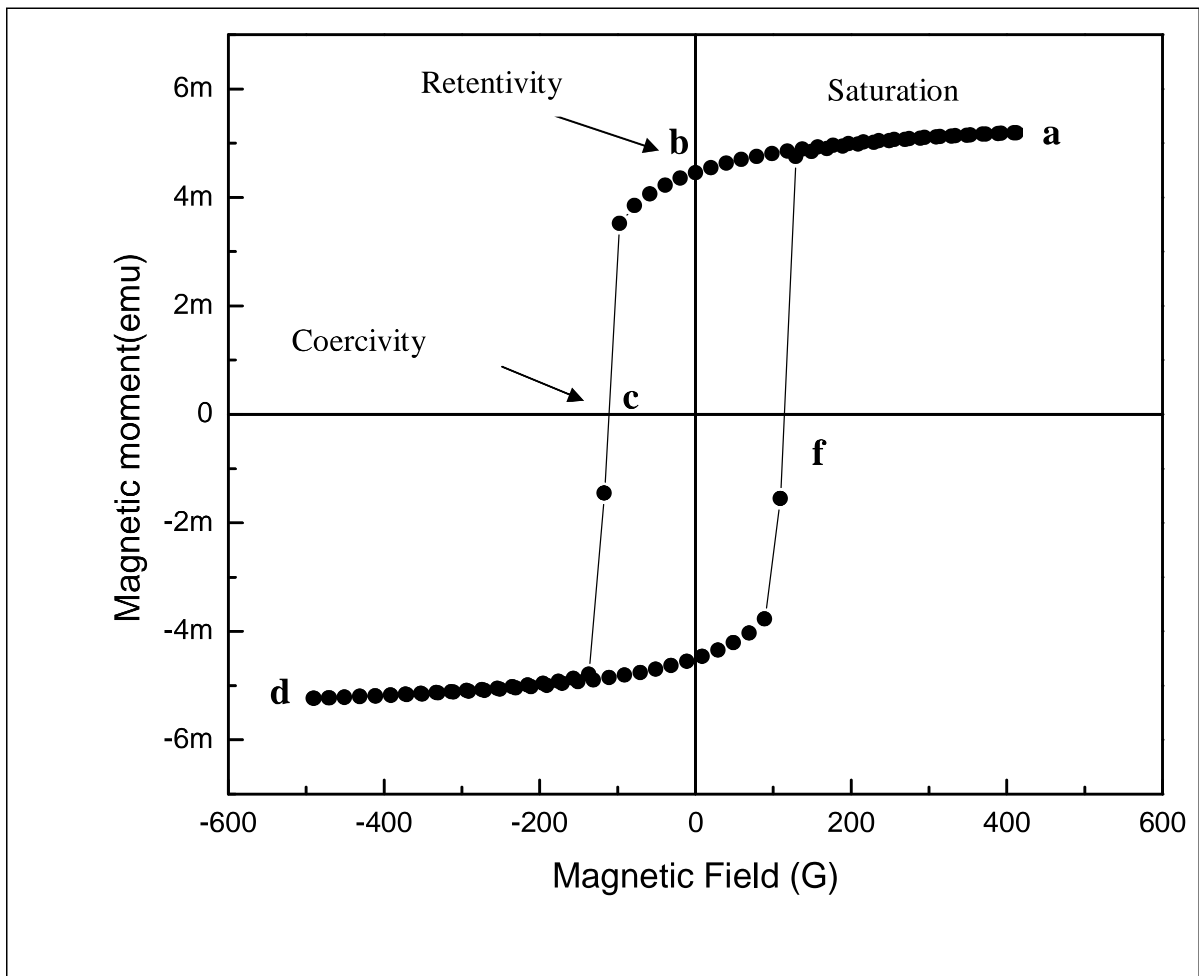

Figure 3.9. Hysteresis curve of a Fe film.

The working principle of VSM is related to Faraday's law of induction. Applying magnetic field causes the sample magnetized, magnetic dipole moments in the sample creates a magnetic field around the sample called magnetic stray field and since the sample

is vibrated in the z direction as a function of time, this stray field as a function of time is sensed from pick up coils and converted into electronic data as a voltage output.

The loop is generated by measuring the magnetic flux of a ferromagnetic material while the magnetizing force is changed. A ferromagnetic material that has never been previously magnetized or has been thoroughly demagnetized will follow the dashed line as H is increased. As the line demonstrates, the greater the amount of current applied (H+), the stronger the magnetic field in the component (B+). At point "a" almost all of the magnetic domains are aligned and an additional increase in the magnetizing force will produce very little increase in magnetic flux.

The material has reached the point of magnetic saturation. When H is reduced to zero, the curve will move from point "a" to point "b." At this point, it can be seen that some magnetic flux remains in the material even though the magnetizing force is zero. This is referred to as the point of retentivity on the graph and indicates the remanence or level of residual magnetism in the material. (Some of the magnetic domains remain aligned but some have lost their alignment.) As the magnetizing force is reversed, the curve moves to point "c", where the flux has been reduced to zero. This is called the point of coercivity on the curve. (The reversed magnetizing force has flipped enough of the domains so that the net flux within the material is zero.) The force required to remove the residual magnetism from the material is called the coercive force or coercivity of the material.

As the magnetizing force is increased in the negative direction, the material will again become magnetically saturated but in the opposite direction (point "d"). Reducing H to zero brings the curve to point "e." It will have a level of residual magnetism equal to that achieved in the other direction. Increasing H back in the positive direction will return B to zero. Notice that the curve did not return to the origin of the graph because some force is required to remove the residual magnetism. The curve will take a different path from point "f" back to the saturation point where it with complete the loop. VSM consist of two movable electromagnets, vibrating unit and the sensing coil. Schematic of VSM and the basic set up is shown in Figure 3.10.

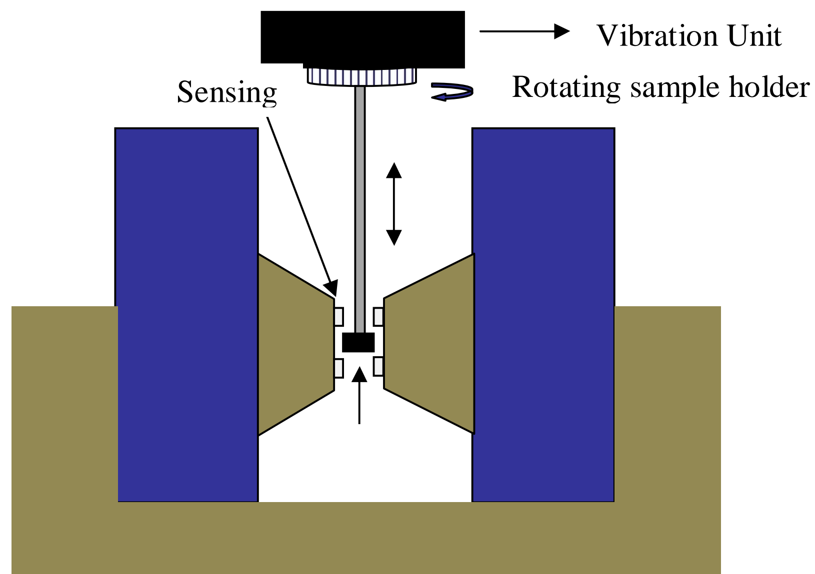

Figure 3.10. Schematic illustration of vibrating sample magnetometer (VSM).

Figure 3.11. Lakeshore 7400 Vibrating Sample Magnetometer (VSM).

Lake shore 7400 series, shown in Figure 3.11. VSM can attain 2 Tesla in the presence of 3 inch gap between magnets and the sample rod vibrates at 84Hz. The moment sensitivity at the ambient temperature is 0.1 μemu and maximum limit at that temperature is 1000 emu.

CHAPTER 4

RESULTS AND DISCUSSION

In this chapter, the structural and the magnetic properties of the trilayers will be presented in detail. The calculation of thickness of magnetically dead layers will be discussed and compared with the model found from XRR. The effect of thermally driven interdiffusion will also be discussed at different annealing temperatures.

4.1. Vibrating Sample Magnetometer (VSM) and MDL Results

4.1.1. $SiO_2/Ta/Ni_{80}Fe_{20}/Ta$

Various thicknesses of 15.2 nm, 7.6 nm, 3.8 nm, 3.04 nm, 2.28 nm and 1.52 nm $Ni_{80}Fe_{20}$ alloy films were deposited between Ta(5nm) and Ta(3nm) metal layers. Magnetic hysteresis loops of these as deposited trilayer structures are shown in Figure 4.1.(a). The easy magnetization of all the samples were reached in applying magnetic field parallel to the films surfaces (J.G.Long, et al. 2001). Saturated magnetic moment of $Ni_{80}Fe_{20}$ is strongly thickness dependent which is normally expected. Since the evolution of magnetic ordering is low in thinner films of $Ni_{80}Fe_{20}$, magnetic moment almost vanishes for 1.52 nm film. The coercivities of soft $Ni_{80}Fe_{20}$ are small (0.8 Oe) (Akther et al. 1997). Nevertheless 1.52 nm $Ni_{80}Fe_{20}$ layer shows big coercivity comparing to thicker films due to discontinuity of the film during deposition. The coercivity does not change for thicker films are due to grain size increment of the film.

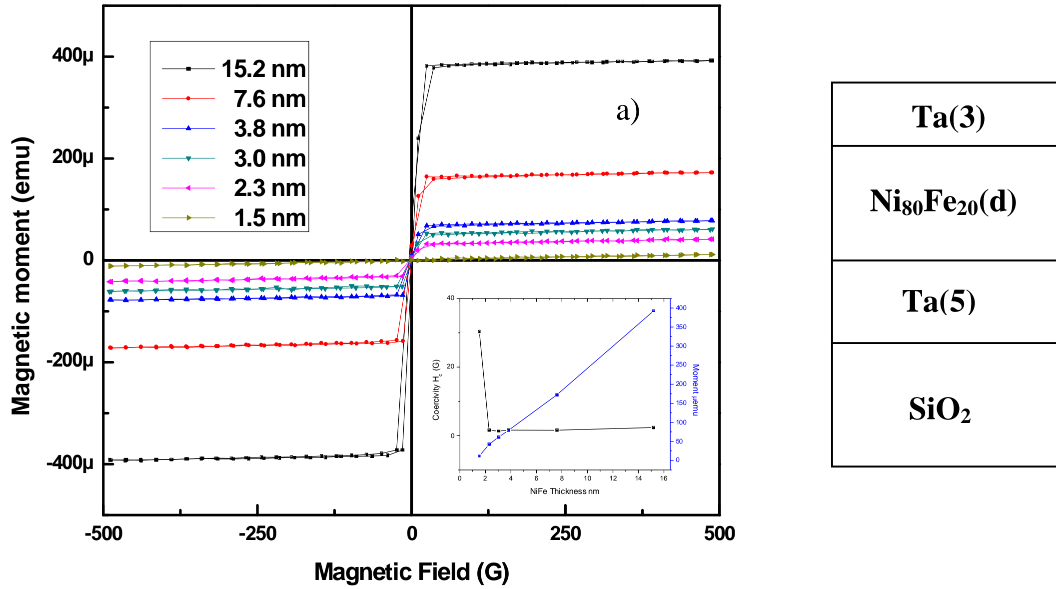

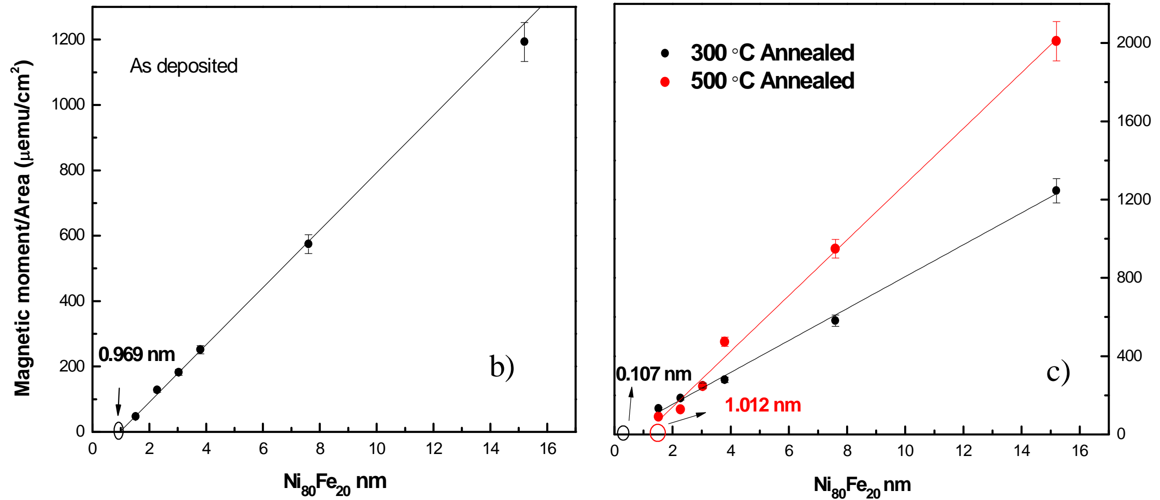

Figure 4.1. a) Magnetic hysteresis loops of as deposited Ta/$Ni_{80}Fe_{20}$(d)/Ta trilayers MDL's at b) 300 ˚C and c) 500 ˚C annealing temperatures.

Thickness of 1.52 nm films behaves as superparamagnetic, because of having almost no remanance and need high applied field to be saturated. Annealing temperatures at 300 ˚C and 500 ˚C distorted the local spin interaction energy in the lattice of the films and decreased the magnetic moment of the alloy films (not shown).

9.7 ± 0.5 Å (MDL) thickness is found for as deposited $Ta(5)/Ni_{80}Fe_{20}(d)/Ta(3)$ trilayer structure shown in Figure 4.1.(b). The MDL decreases to 1 ± 0.5 Å at 300 ˚C and increased to 10 ± 0.5 Å at 500 ˚C shown in the same Figure 4.1. (c).

Thickness of MDL in general increases with annealing temperatures (Liebermann, et al. 1970). However MDL thickness reduces from 9 ± 0.5 Å to 1 ± 0.5 Å at 300 ˚C. Reduction at 300 ˚C might be crystallization of both Ta-$Ni_{80}Fe_{20}$ and $Ni_{80}Fe_{20}$-Ta interfaces. Defects or magnetic impurities may also be reduced at this annealing temperature. Thickness of MDL increases to 10 ± Å at 500 ˚C is due to thermally driven interdiffusion of Ta atoms into $Ni_{80}Fe_{20}$ alloy. Saturation magnetization of as deposited $Ni_{80}Fe_{20}$ film can be obtained from slope of linear fits in Figure 4.1. (b). Saturation magnetization is found to be 878 (emu/cm^3) which is close to bulk $Ni_{80}Fe_{20}$ alloy (800 emu/cm^3).

4.1.2. $SiO_2/Ta/Ni_{80}Fe_{20}/Ta_2O_5$

In this part, we will see the effect of Ta_2O_5 insulator on the magnetic properties of $Ni_{80}Fe_{20}$ film. Figure 4.2 shows the anisotropy measurement for the $Ni_{80}Fe_{20}$ film. From 0-180 degree saturation magnetic moment changes 100-104 μ emu which is quite low that means there is no magnetic anisotropy for $Ni_{80}Fe_{20}$ film.

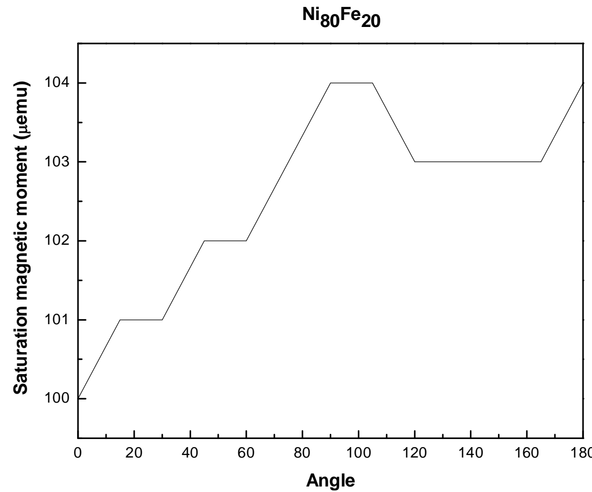

Figure 4.2. Angle dependence of saturation magnetic moment for the $Ni_{80}Fe_{20}$ film.

Figure 4.3.(a) shows the magnetic hysteresis of SiO_2/Ta/$Ni_{80}Fe_{20}$(d)/Ta_2O_5 with various thickness. The saturated magnetic moment decreases when the samples are annealed at 300 ˚C and 500 ˚C (not shown). The change of coercivity against the thickness of variation is as same as Ta/$Ni_{80}Fe_{20}$/Ta structure. 1.52 nm thickness of $Ni_{80}Fe_{20}$ shows big coercivity is again due to small grain size during the first stage of deposition.

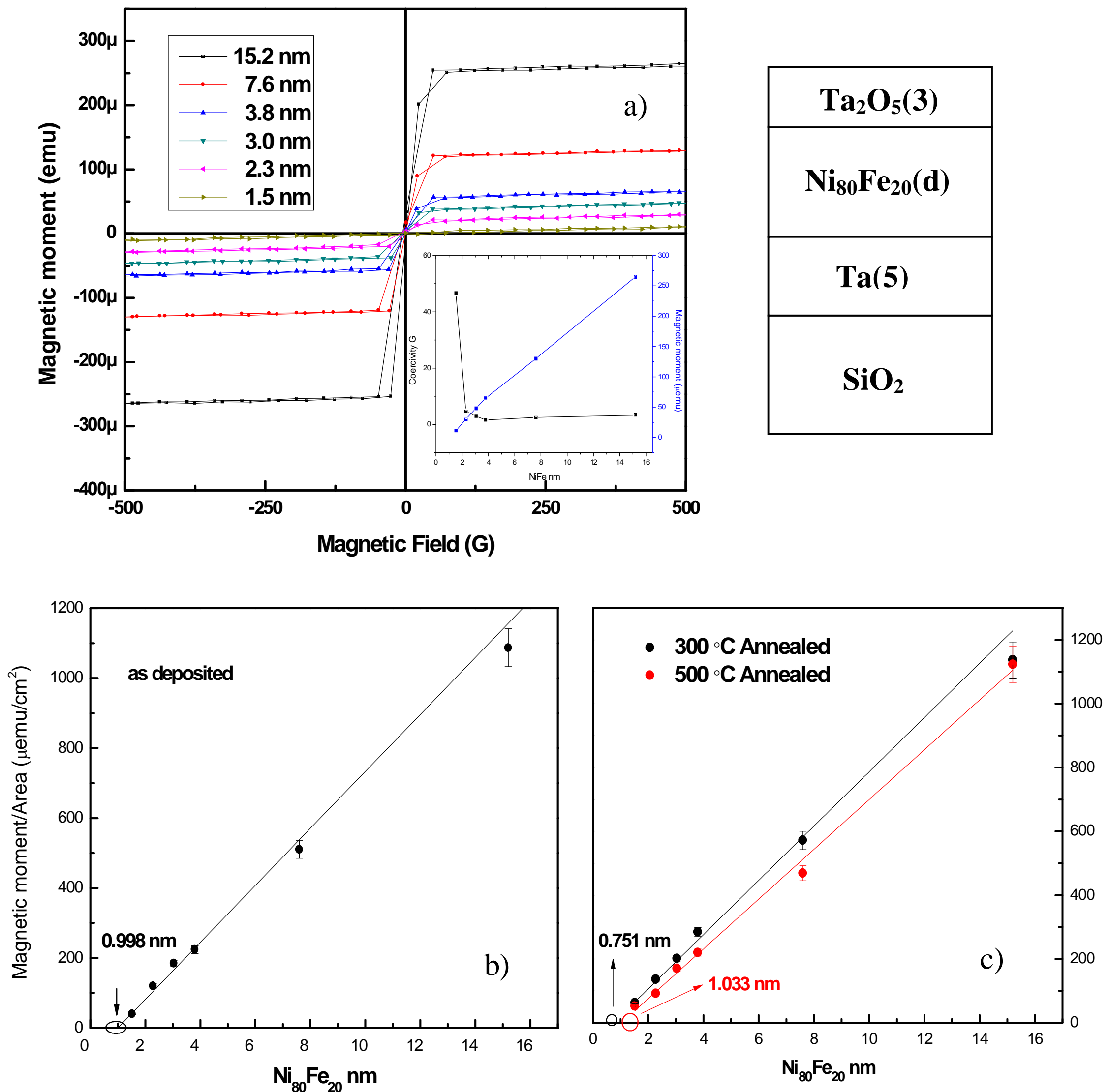

Figure 4.3. a) Magnetic hysteresis loops of as deposited Ta/$Ni_{80}Fe_{20}$(d)/Ta_2O_5 trilayers MDL's at the b) 300 ˚C and c) 500 ˚C annealing temperatures.

The coercivity change with respect to thickness of the film is as same as $Ni_{80}Fe_{20}$ between Ta layers. 1.52 nm $Ni_{80}Fe_{20}$ film has almost no remnant magnetic moment and needs high applied magnetic field to be saturated.

These properties reveal that $Ni_{80}Fe_{20}$ shows superparamagnetic behavior at this thickness and the grain size of the thin $Ni_{80}Fe_{20}$ particles can be calculated by Langevin function. The maximum saturation magnetic moment (easy axis) is needed for calculating MDL. Hence, it is important to check the anisotropy for ferromagnetic films. MDL calculations for as deposited SiO_2/Ta/$Ni_{80}Fe_{20}$(d)/Ta_2O_5 is found to be 10 ± 0.5 Å shown in Figure 4.3.(b), comparing to as deposited Ta/$Ni_{80}Fe_{20}$/Ta structure there is 0.3 Å MDL thickness increment is measured at the interface of $Ni_{80}Fe_{20}$/Ta_2O_5.

MDL thickness decreases at 300 ˚C are due to improvement of interfaces of $Ni_{80}Fe_{20}$ film. Comparing to 300 ˚C annealed Ta/$Ni_{80}Fe_{20}$/Ta structure, MDL thickness is more than 6 ± 0.5 Å for 300 ˚C annealed Ta/$Ni_{80}Fe_{20}$/Ta_2O_5 structure. This states that annealing at 300 ˚C, MDL increases a lot at the interface of $Ni_{80}Fe_{20}$/Ta_2O_5.

Interdiffusion is dominated at 500 ˚C and MDL increases to 10 ± 0.5 Å which is more than as deposited MDL thickness of the stack shown in Figure 4.3.(c). MDL thickness at 500 ˚C is more than the MDL thickness 500 ˚C for Ta/$Ni_{80}Fe_{20}$/Ta layer indicating intermixing at $Ni_{80}Fe_{20}$/Ta_2O interface increases at higher annealing temperatures. Saturated magnetization of $Ni_{80}Fe_{20}$ in as deposited Ta/$Ni_{80}Fe_{20}$/Ta_2O_5 is 814 (emu/cm^3) which is almost as same as deposited Ta/$Ni_{80}Fe_{20}$/Ta structure.

4.1.3. SiO_2/Ta_2O_5/$Ni_{80}Fe_{20}$/Ta_2O_5

Ta_2O_5 is used in order to understand seed layer effect on the MDL thickness and corresponding magnetic property of $Ni_{80}Fe_{20}$. Figure 4.4. (a) shows the magnetic hysteresis loops for the structure. Since the $Ni_{80}Fe_{20}$ layer is now deposited on rough Ta_2O_5 surface, the magnetic properties of the $Ni_{80}Fe_{20}$ change. This change can be seen in the insert of Figure 4.4. (a) that the coercivity of the film first rises and then drops to minimum for 4 nm of $Ni_{80}Fe_{20}$ due to oxygen interaction at the Ta_2O_5/$Ni_{80}Fe_{20}$ interface. 1.52 nm $Ni_{80}Fe_{20}$ film

has very small coercivity comparing to $Ni_{80}Fe_{20}$ in Ta-Ta and Ta-Ta_2O_5 trilayers indicating $Ni_{80}Fe_{20}$ films are more uniform at the first stage of deposition.

In Figure 4.4.b), it is seen that as deposited MDL thickness is quite thin (1.8 ± 0.5 Å) comparing to as deposited Ta/$Ni_{80}Fe_{20}$/Ta_2O_5 (9.98 ± 0.5 Å) structure revealing that Ta seed layer creates more magnetic dead layer comparing to Ta_2O_5 seed layer.Thermally driven interdiffusion is both obtained at 300 ˚C and 500 ˚C annealing temperatures shown in Figure 4.4.c).

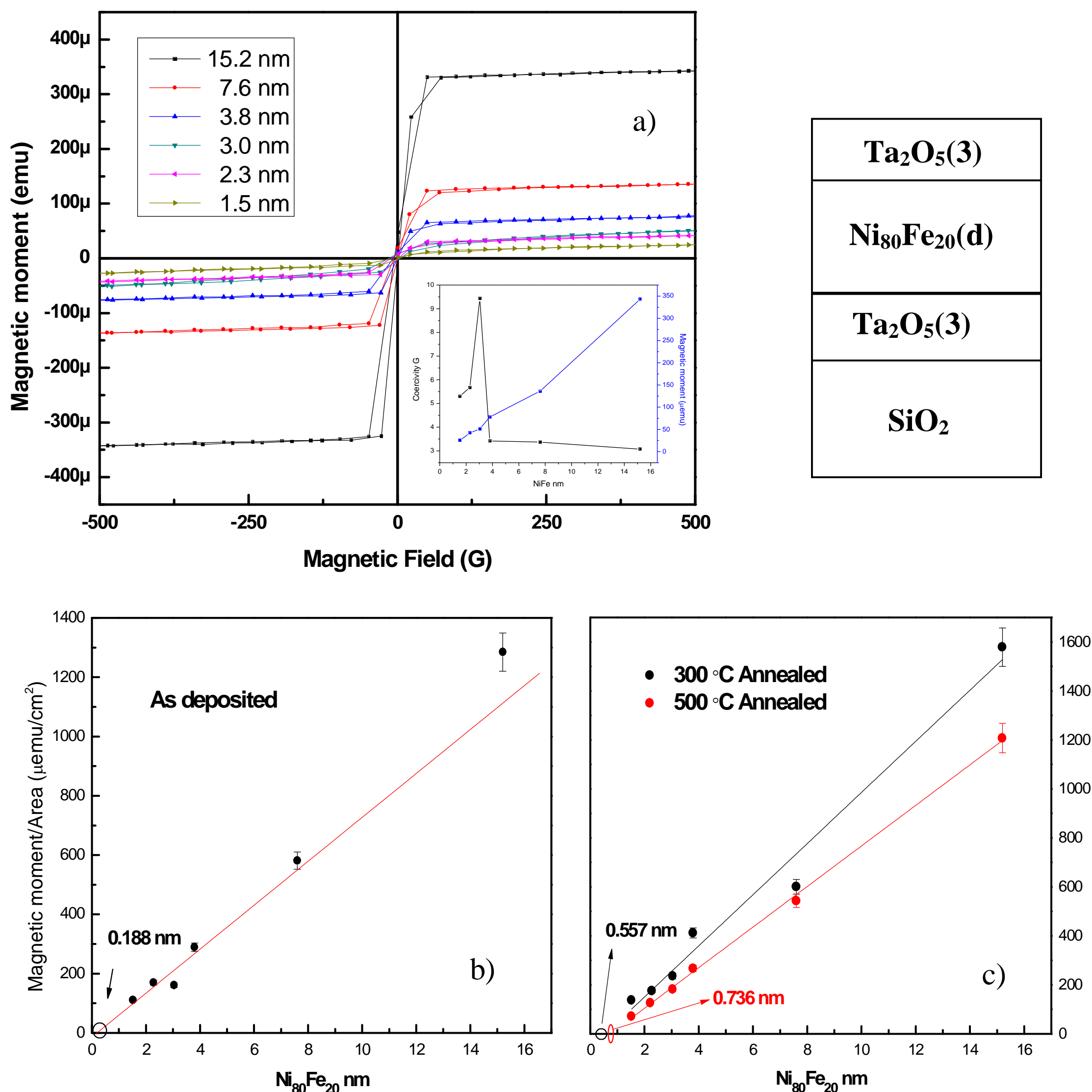

Figure 4.4. a) Magnetic hysteresis loops of as deposited Ta_2O_5/$Ni_{80}Fe_{20}$(d)/Ta_2O_5 trilayers and MDL's at b) 300 ˚C and c) 500 ˚C annealing temperatures.

The possible increasing MDL thickness at different annealing temperature is due to oxygen interdiffusion at the interface of $Ta_2O_5/Ni_{80}Fe_{20}$ layers. MDL thickness of $Ta_2O_5/Ni_{80}Fe_{20}/Ta_2O_5$ is more both at 300 ˚C and 500 ˚C annealing temperatures indicating Ta seed layer creating deader layer comparing to Ta_2O_5 insulator. The explanation of why Ta creates more MDL can be explained as of surface free energy of Ta increment with increasing temperatures and this leads more interdiffusion from Ta into $Ni_{80}Fe_{20}$ alloy.

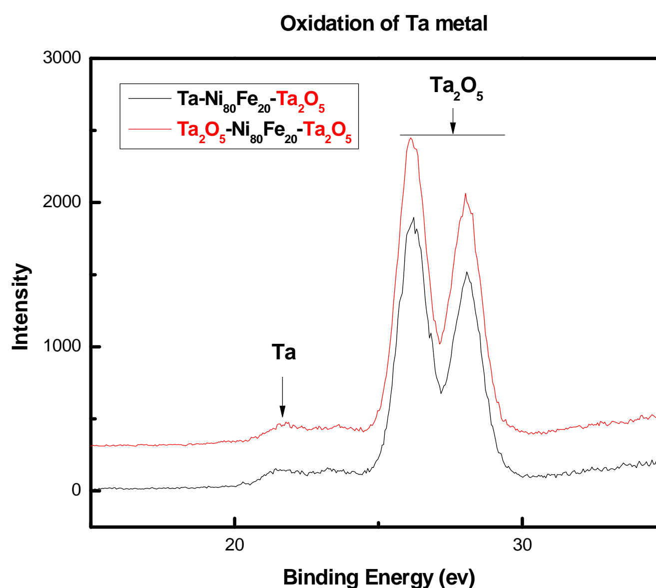

Figure 4.5. XPS measurements of Ta-$Ni_{80}Fe_{20}$-Ta_2O_5 and Ta_2O_5-$Ni_{80}Fe_{20}$-Ta_2O_5 trilayers.

Very small MDL for the Ta_2O_5-$Ni_{80}Fe_{20}$-Ta_2O_5 comparing to Ta-$Ni_{80}Fe_{20}$-Ta_2O_5 may be understood form XPS study at the $Ni_{80}Fe_{20}/Ta_2O_5$ interface. Both samples are oxidized to a large extend as seen in Figure 4.5. There is a small Ta peak for both structures indicating that there exits at least a monolayer of Ta for the cap Ta_2O_5 layers which causes more MDL.

4.1.4. $SiO_2/Ta/Ni_{80}Fe_{20}/Al_2O_3$

One of the most extensively used amorphous tunnel barrier in spintronics devices is aluminum oxide because of its suitability for forming a thin (10 Å), smooth and dense barrier layer, along with its relatively bonding energy with oxygen (>3 ev) (Park, et al. 2006). To see the effect of cap Al_2O_3 insulator on MDL thickness, we further studied the magnetically dead layers at the interface of $Ni_{80}Fe_{20}/Al_2O_3$. Magnetic hysteresis data is shown in Figure 4.6. a) Magnetic moment of $Ni_{80}Fe_{20}$ is thickness dependent.

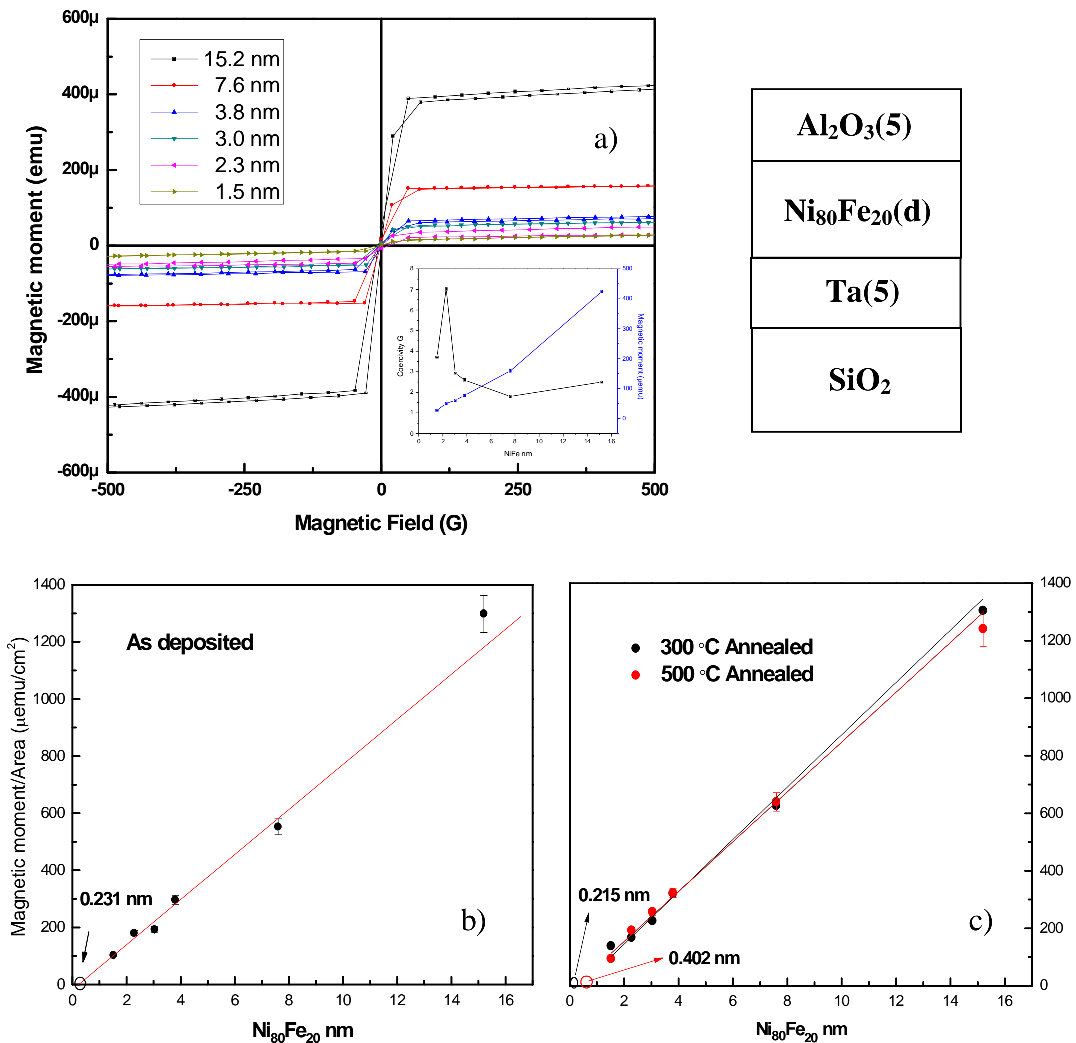

Figure 4.6. a) Magnetic hysteresis loops of as deposited $Ta/Ni_{80}Fe_{20}(d)/Al_2O_3$ trilayers MDL's at the b) 300 ˚C and c) 500 ˚C annealing temperatures.

The coercivity (H_c) of the film at the first stage of deposition is so small comparing to coercivity of $Ni_{80}Fe_{20}$ in Ta-$Ni_{80}Fe_{20}$-Ta and Ta-$Ni_{80}Fe_{20}$-Ta_2O_5 trilayer structures. The trend of the coercivity change with respect to film thickness may be attributed to uniform film deposition.

MDL thickness of as deposited structure is measured as 2.3 ± 0.5 Å shown in Figure 4.5.(b). Comparing to SiO_2/Ta/$Ni_{80}Fe_{20}$/Ta structure, SiO_2/Ta/$Ni_{80}Fe_{20}$/Al_2O_3 has 7 ± 0.5 Å less MDL thickness indicating cap Al_2O_3 creates significantly less magnetic dead layer. Since Ta has more valence electrons comparing to Al_2O_3, Ni reduces more magnetic moment due to more shared electron in its d orbital's. The thickness of MDL first decreases at 300 ˚C to 2.5 ± 0.5 Å and then increases to 4 ± 0.5 Å at 500 ˚C shown in Figure 4.5.(c). Thermally driven interdiffusion increases at this temperature.

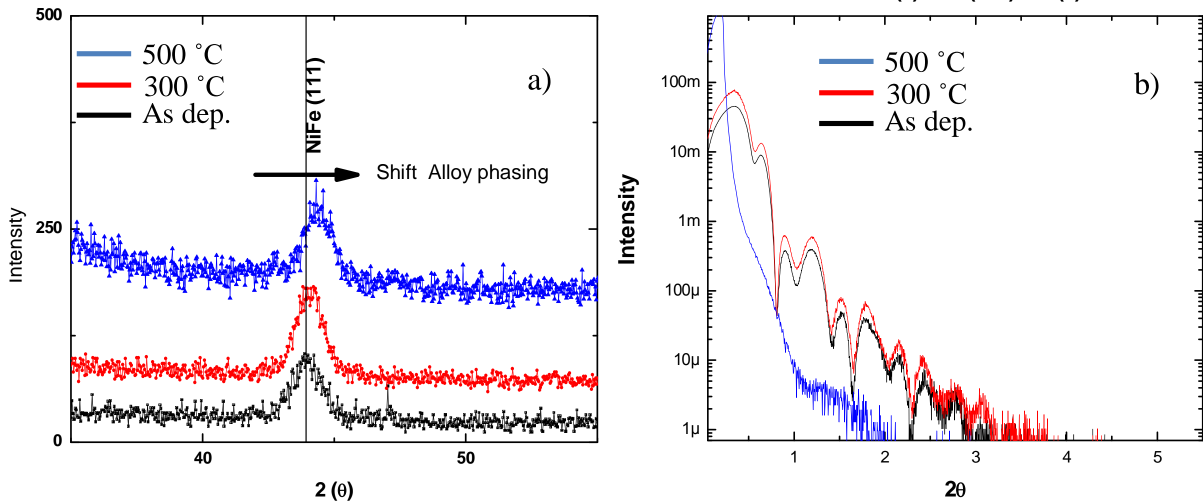

Figure 4.7. a) XRD patters and b) XRR measurements for Ta/$Ni_{80}Fe_{20}$/Al_2O_3 multilayer.

Thermally driven interdiffusion at 500 ˚C can also be understood in both XRD and XRR data shown in Figure 4.7. According to XRD patterns for the Ta/$Ni_{80}Fe_{20}$/Al_2O_3 multilayer shown in Figure 4.7. (a), NiFe (111) peak does not shift for as deposited and 300 ˚C multilayers however for 500 ˚C annealed samples peak shifts can be seen which is also shown in Table 4.1. The shift in the Ni peak may be explained as alloy phasing (Ding, et al. 2009) due to interdiffusion. MDL thickness doubles at 500 ˚C due to interdiffusion.

Table 4.1. Table of XRD specifications and MDL's of $Ta/Ni_{80}Fe_{20}/Al_2O_3$ multilayer.

Specifications	As Deposited	300 ˚C	500 ˚C
Peak Pos.	44.048	44.076	44.398
FWHM	1.379	1.392	0.847
Grain Size (nm)	6.2	6.2	10.1
MDL (Å)	2.3	2.15	4.0

Thermally driven interdiffusion cal also be understood from XRR measurement shown in Figure 4.7. (b). Kiessing fringes at 500 ˚C disappears this means interdiffusion increase the roughness of interlayer so interfaces of $Ni_{80}Fe_{20}$ film.

4.1.5. $SiO_2/Al_2O_3/Ni_{80}Fe_{20}/Ta$

The effect of Al_2O_3 as a seed layer is studied. Magnetic hysteresis loops for the $Al_2O_3/Ni_{80}Fe_{20}/Ta$ structure are shown in Figure 4.8.(a). The magnetic moment of the ferromagnetic alloy is thickness dependent. The coercivity change with respect to different thickness of film is different comparing to $Ta/Ni_{80}Fe_{20}/Al_2O_3$ structure. Coercivity increases then drops is due to $Ni_{80}Fe_{20}$ film is on top of amorphous layer and surface is rough which effects the crystallization of the $Ni_{80}Fe_{20}$ film during growth. MDL thickness for as deposited structures is shown in Figure 4.8.(b).

MDL thickness is more than as deposited $Ta/Ni_{80}Fe_{20}/Al_2O_3$. Since the amorphous Al_2O_3 is deposited on amorphous SiO_2, this potentially creates more rough surfaces for the seed Al_2O_3 to increase the interdiffusion probability at the interface with $Ni_{80}Fe_{20}$. MDL thickness decreases at 300 ˚C is due to improvement of seed Al_2O_3 insulator at the interface, however the MDL thickness increases to 4.7 ± 0.5 Å at 500 ˚C shown in Figure 4.8.(c). At this temperature thermally interdiffusion increases a lot. Table 4.2. shows the MDL thickness of all different structures. As it is seen in the table that annealing decreases the MDL thickness except for the $Ta_2O_5/Ni_{80}Fe_{20}/Ta_2O_5$ structure. MDL thickness increases for all stacks at 500 ˚C.

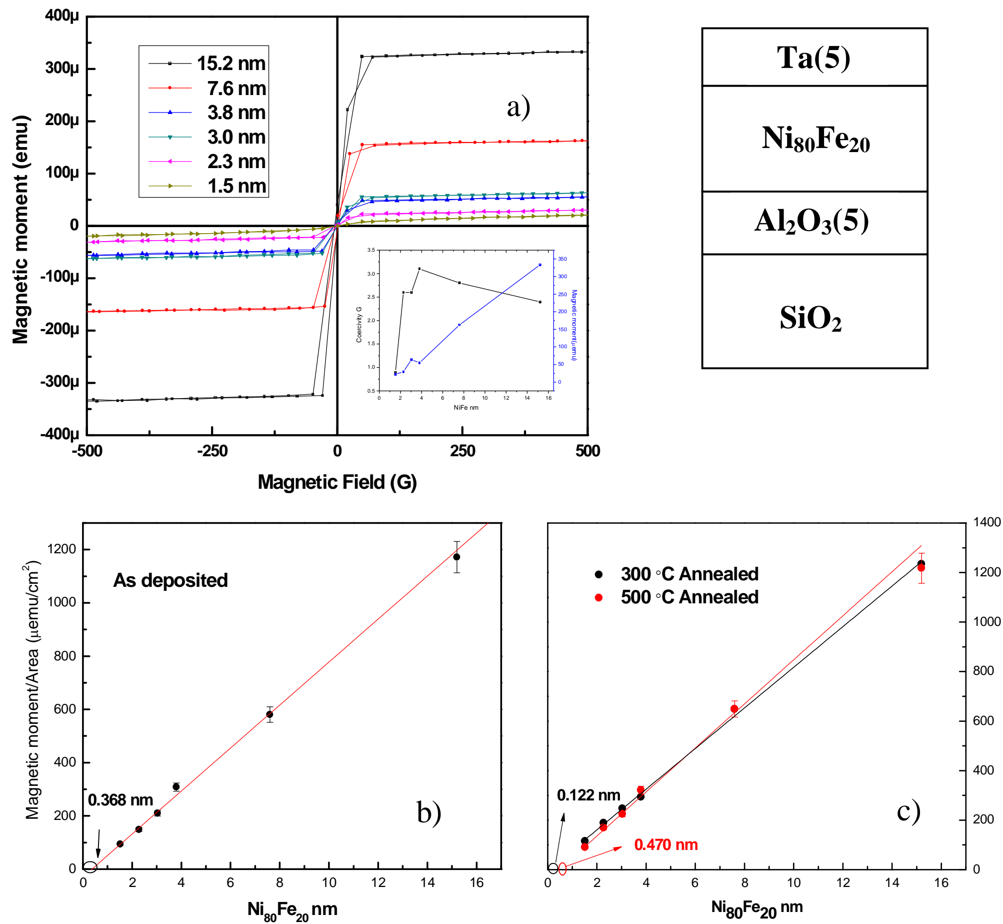

Figure 4.8. a) Magnetic hysteresis loops of as deposited $Al_2O_3/Ni_{80}Fe_{20}(d)/Ta$ trilayers MDL's at the b) 300 ˚C and c) 500 ˚C annealing temperatures.

Table 4.2. Magnetic dead layers of $Ni_{80}Fe_{20}$ for each stack.

Multilayers	As Deposited (Å)	300 ˚C (**Å**)	500 ˚C (**Å**)
Al_2O_3-$Ni_{80}Fe_{20}$-Ta	3.6	1.2	4.7
Ta-$Ni_{80}Fe_{20}$-Ta	9.7	1.0	10.1
Ta-$Ni_{80}Fe_{20}$-Ta_2O_5	9.9	7.5	10.3
Ta-$Ni_{80}Fe_{20}$-Al_2O_3	2.3	2.15	4.0
Ta_2O_5-$Ni_{80}Fe_{20}$-Ta_2O_5	1.9	5.60	7.3

4.3. X-Ray Reflectivity Measurements Results (XRR)

4.3.1. SiO_2/Ta(5nm)/$Ni_{80}Fe_{20}$(7.6nm)/Ta(3nm)

X ray reflectivity measurement was performed for the SiO_2/Ta(5nm)/$Ni_{80}Fe_{20}$ (7.6nm)/Ta(3nm) structure shown in Figure 4.9. The measured data was fit by considering different combinations of roughness, densities and thickness of the layers. In order to fit the measured data, 2.4 nm Ta_2O_5 oxidized surface layer is taken into account. Thickness of $Ni_{80}Fe_{20}$ alloy is found to be 7.22 nm which is very close to the deposition rate for the 10 min (7.6 nm) film measured from thickness monitor.

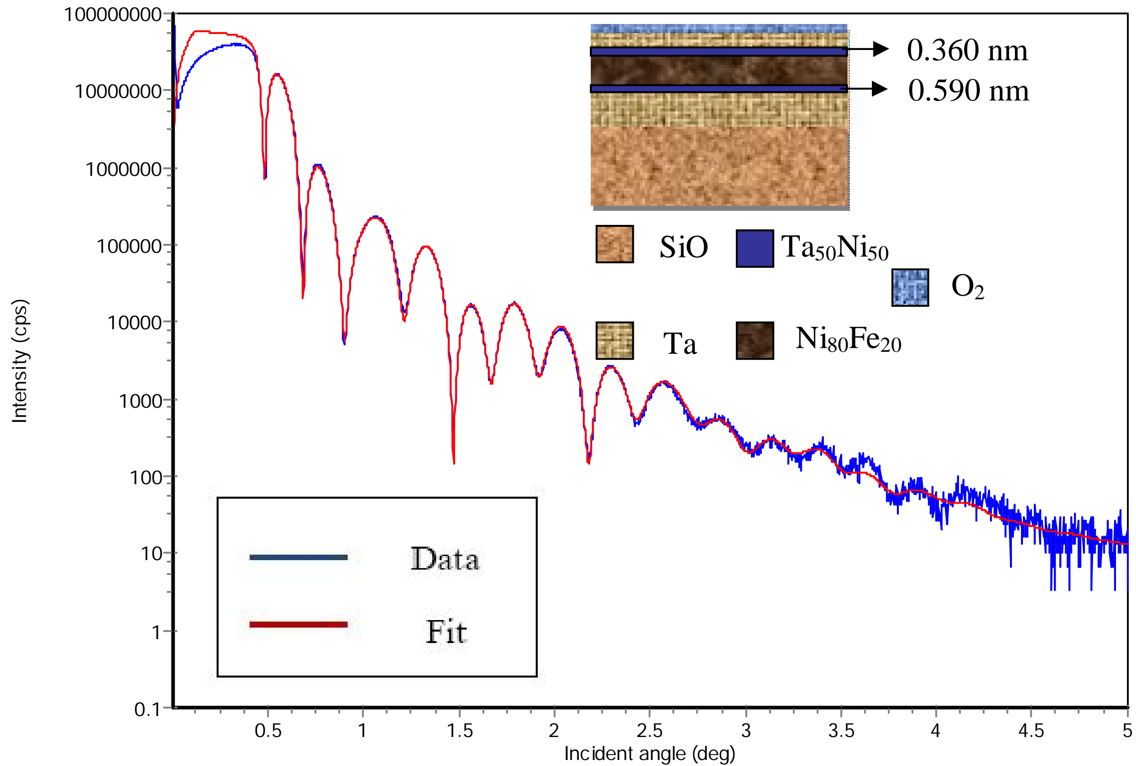

Figure 4.9. XRR measurement of SiO_2/Ta(5nm)/$Ni_{80}Fe_{20}$(7.6nm)/Ta(3nm) layer.

In order to fit the measured data, 5.8 nm Ta for bottom and 2.3 nm Ta for the top layers are used in the model. Different combination of atomic percentage is tried at the

interface of $Ni_{80}Fe_{20}$ film and in the end, it was found that $Ta_{0.5}Ni_{0.5}$ layers fit the measured data well. The important part is to determine the thickness of these inter layers which are attributed as magnetic dead layers. The fit model states that there is more interdiffused layer at the interface of $Ta/Ni_{80}Fe_{20}$ (6 Å) than at the interface $Ni_{80}Fe_{20}/Ta$ (3.6Å) which is consistent with the idea of surface free energy factor of the Ta metal. The total thickness of interdiffused layers is 9.5 Å which is quite close the MDL thickness (9.7 Å) of as deposited $SiO_2/Ta/Ni_{80}Fe_{20}/Ta$ structure found from magnetization data.

Table 4.3. Segmented fit model of SiO_2/Ta(5nm)/$Ni_{80}Fe_{20}$(7.6nm)/Ta(3nm).

Layer	**Layer Description**	**Density(g/cm3)**	**Thickness(nm)**	**Roughness(nm)**
Substrate	SiO_2	3.727	550000	0.253
1	Ta	15.202	5.891	0.42
2	**Ta 0.50 Ni 0.50**	11.36	**0.59**	0.497
3	Ni 0.80 Fe 0.20	8.686	7.233	0.587
4	**Ta 0.50 Ni 0.50**	15.686	**0.36**	0.927
5	Ta	14.926	2.374	0.49
6	Ta_2O_5	7.563	2.464	0.629

Another possible reason to explain why Ta makes interalloy especially with Ni instead of Fe is due to high concentration 80% of Ni in the $Ni_{80}Fe_{20}$ alloy.

4.3.2. SiO_2 /Ta(5nm)/$Ni_{80}Fe_{20}$(7.6nm)/Ta_2O_5(3nm)

In this case, to see the effect of cap insulator layer on the interdiffused layers, XRR measurement was performed that is shown in Figure 4.8. We have six modeled layers for this sample. The top layer is covered by oxidized Ta with the percentage of (% 35 Ta and % 65 O_2). Thickness of $Ni_{80}Fe_{20}$ from XRR data (7.9nm) is consistent with the 7.6 nm $Ni_{80}Fe_{20}$ thickness.

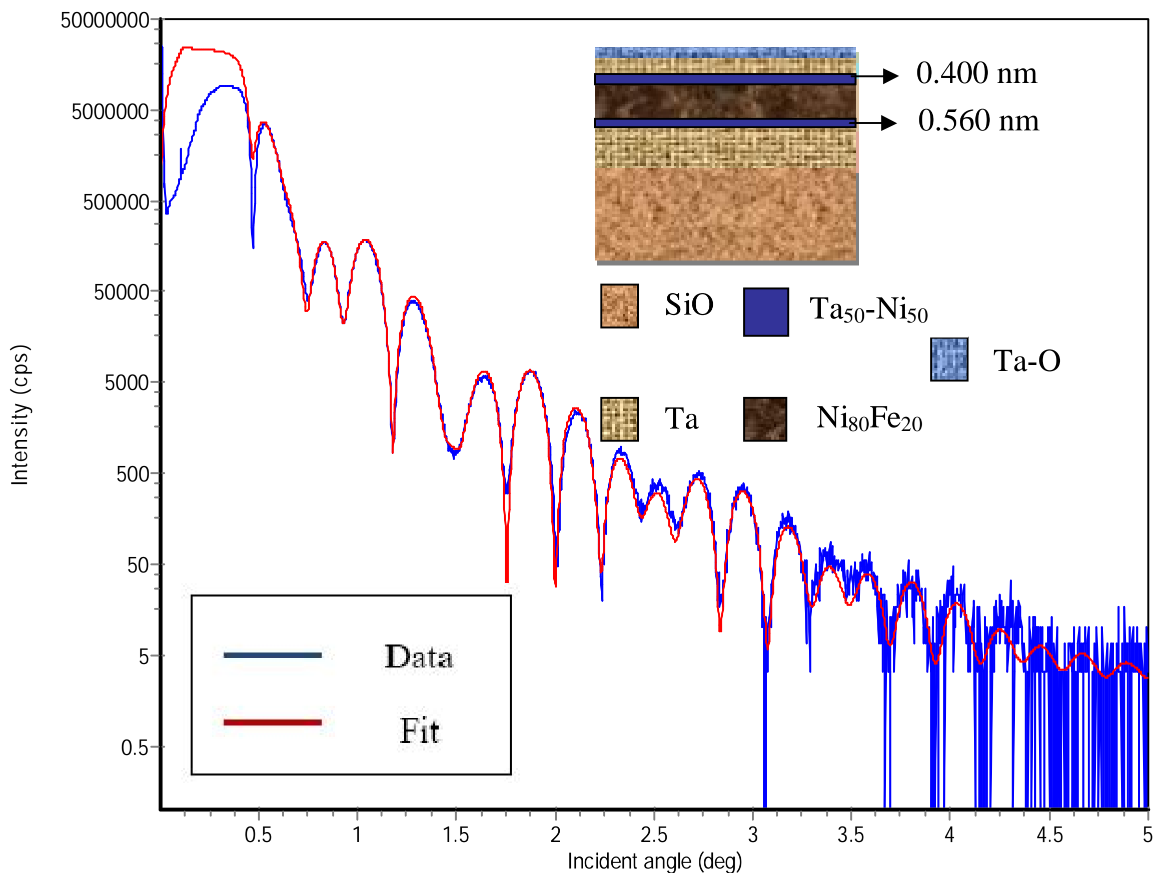

Figure 4.10. XRR measurement of SiO_2/Ta(5nm)/$Ni_{80}Fe_{20}$(7.6nm)/Ta_2O_5(3nm) layer.

According to segmented fit model shown in Table 4.4, there is 5.6 Å interdiffused alloy formation at the Ta/$Ni_{80}Fe_{20}$ whereas the interdiffused alloy at the $Ni_{80}Fe_{20}$/Ta_2O_5 is 4 Å. Total thickness of inderdiffused alloys is 9.6 Å and consistent with the thickness found from magnetization data of as deposited Ta/$Ni_{80}Fe_{20}$/Ta_2O_5 (9.8 Å).

Table 4.4. Segmented fit model of SiO_2/Ta(5nm)/$Ni_{80}Fe_{20}$(7.6nm)/Ta_2O_5(3nm).

Layer	Layer Description	Density (g/cm3)	Thickness (nm)	Roughness (nm)
Substrate	SiO_2	3.592	550000	0.298
1	Ta	14.375	4.842	0.617
2	**Ta 0.50 Ni 0.50**	18.139	**0.56**	1.021
3	Ni 0.80 Fe 0.20	8.686	7.975	0.84
4	**Ta 0.50 Ni 0.50**	6.382	**0.40**	0.674
5	Ta	12.746	2.083	0.428
6	Ta 0.35 O 0.65	5.382	4.532	0.334

It is also confirmed from XRR data that Ta creates more interdiffused layer which is also consistent with the magnetization data. The same reason can be expressed by considering the Ta surface free energy. XRR data reveals that cap Ta_2O_5 layer creates more interdiffused layer (4 Å) comparing to cap Ta layer (3.6 Å) which is also confirmed from MDL calculations found from magnetization data.

4.3.3. SiO_2/Ta_2O_5(3nm)/$Ni_{80}Fe_{20}$(7.6nm)/Ta_2O_5(3nm)

XRR measurements on SiO_2/Ta_2O_5(3nm)/$Ni_{80}Fe_{20}$(7.6nm)/Ta_2O_5(3nm) trilayer structure is shown in Figure 4.11. The Kiessing fringes have more re-entrants comparing to previous structures due to having both seed and cap Ta_2O_5 insulator structures producing

more absorption sides for the X ray radiation. According to XRR data ~2 Å total non magnetic layers are found which is almost the same thickness of magnetic dead layer found from magnetization (1.8 $^{+}/_{-}$ 0.5 Å). According to segmented fit model shown in Table 4.5., there is 0.1 Å non magnetic interdiffused layer at the interface of $Ta_2O_5/Ni_{80}Fe_{20}$ layer and ten times thicker 1 Å interdiffused MDL structure at the interface of $Ni_{80}Fe_{20}/Ta_2O_5$.

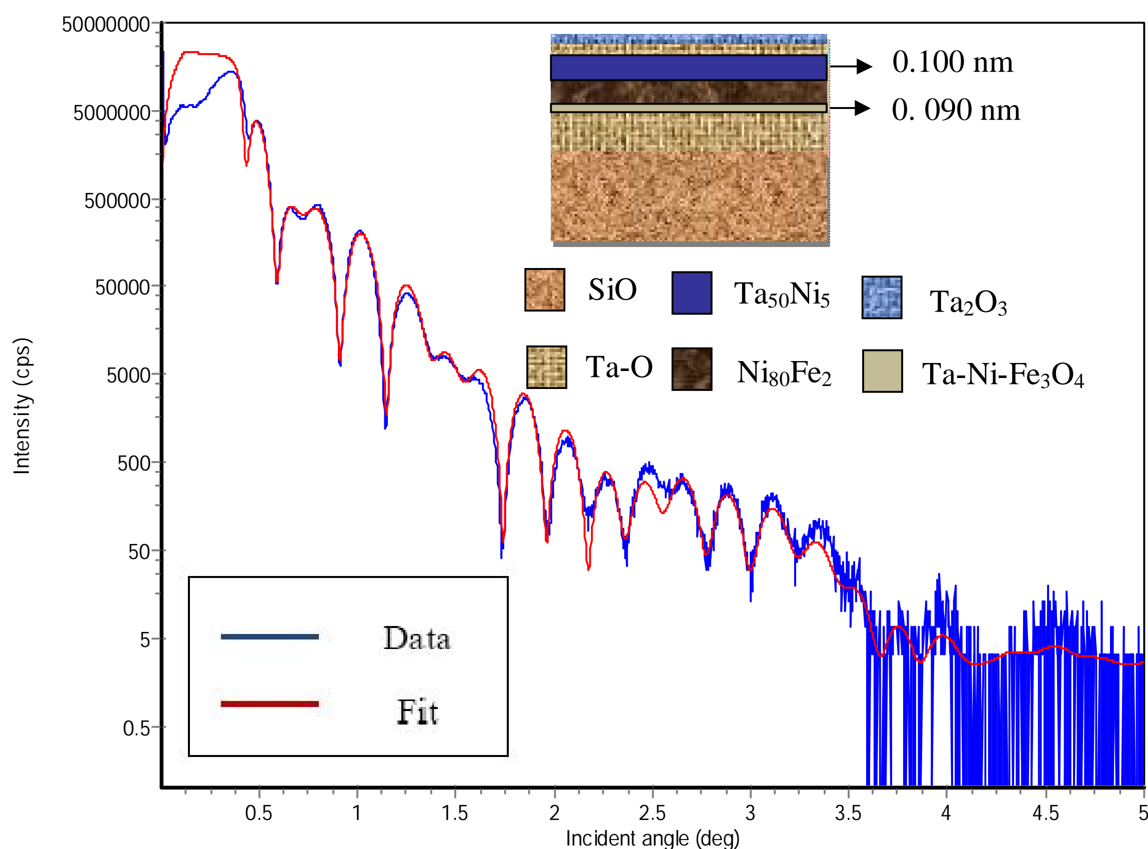

Figure 4.11. XRR measurement of SiO_2/Ta_2O_5(3nm)/$Ni_{80}Fe_{20}$(7.6nm)/Ta_2O_5(3nm) layer.

Surprisingly, seed Ta_2O_5 layer does not produce much more MDL thickness comparing to Ta layer. This fact is also consistent with the MDL calculation. This can be understood as oxygen has less surface free energy compared to Ta. Hence the interdiffusion of oxygen is less than Ta seed layer. Thickness of 7.5 nm $Ni_{80}Fe_{20}$ is consistent with the 7.6 nm $Ni_{80}Fe_{20}$ found from thickness monitor. Total interdiffused layer

is 1.9 Å and roughly consistent with the measured 1.8 Å calculated magnetic dead layers from magnetization of as deposited structure.

Table 4.5. Segmented fit model of $SiO_2/Ta_2O_5(3)/Ni_{80}Fe_{20}(7.6)/Ta_2O_5(3)$.

Layer	Layer Description	Density (g/cm3)	Thickness (nm)	Roughness (nm)
Substrate	SiO_2	1.018	550000	0.382
1	Ta	12.2	2.142	0.297
2	Ta 0.50 O 0.50	7.78	4.08	0.231
3	**Ta 0.34** **Ni 0.33** **Fe_3O_4 0.33**	5.494	**0.09**	0.428
4	Ni 0.70 Fe 0.30	7.604	7.518	0.523
5	**Ta 0.50** **Ni 0.50**	7.548	**0.10**	0.781
6	Ta	12.515	2.285	0.486
7	Ta 0.40 O 0.60	6.931	2.821	0.759
8	O	4.35	1.726	0.412

4.3.4. $SiO_2/Al_2O_3/Ni_{80}Fe_{20}/Ta$

After studying the XRR data for Ta_2O_5 insulator, Al_2O_3 insulator was used as a seed layer to determine the interdiffused layer at the interfaces of $Ni_{80}Fe_{20}$ alloy shown in Figure 4.12. In order to fit the XRR data, various stacks with different atomic percentages were considered. The interdiffused layer at $Al_2O_3/Ni_{80}Fe_{20}$ interface is composed of Ni (0.50), Al

(0.25), Fe (0.10), O_2 (0.15) shown in Table 4.6. The total non magnetic layer is 2.62 Å and so close to MDL thickness found from magnetization data (2.65 Å).

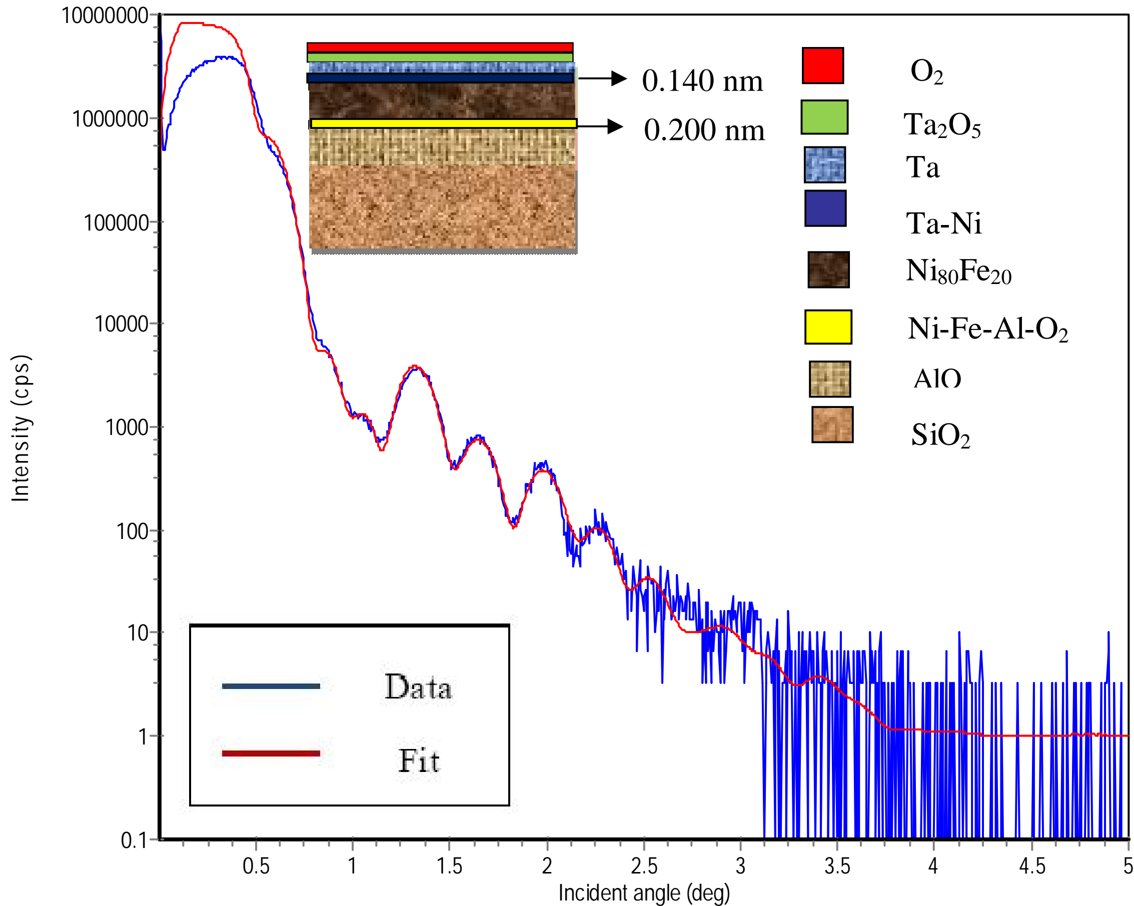

Figure 4.12. XRR measurement of SiO_2/Al_2O_3(5nm)/$Ni_{80}Fe_{20}$(7.6nm)/Ta(5nm) layer.

As we stated at the calculation of MDL thickness for this structure that the interaction between SiO_2 and Al_2O_3 should create rough Al_2O_3 surface which enhance the interdiffusion probability at the interface. This argument is confirmed by the XRR data. To fit the measured data, the oxidized surface is considered and O_2 layer is put. We have nice Kiessing fringes in the reflectivity data and the measured data is well fitted due to our segmented fit model.

Table 4.6. Segmented fit model of SiO_2/Al_2O_3(5nm)/$Ni_{80}Fe_{20}$(7.6nm)/Ta(5nm).

Layer	Layer Description	Density(g/cm3)	Thickness(nm)	Roughness(nm)
Substrate	SiO_2	0.678	450000	0.338
1	Al 0.20 O 0.80	0.919	3.874	0.65
2	**Ni 0.50** **Al 0.25** **Fe 0.10** **O 0.15**	3.641	**0.200**	0.67
3	Ni 0.80 Fe 0.20	7.439	7.056	0.605
4	**Ta 0.70** **Ni 0.30**	14.971	**0.140**	0.388
5	Ta	13.551	5.149	0.606
6	Ta 0.35 O 0.65	6.091	2.38	0.358
7	O_2	0.736	1.592	0.245

4.3.5. SiO_2/Ta(5nm)/$Ni_{80}Fe_{20}$(7.6nm)/Al_2O_3(5nm)

Figure 4.13 shows the XRR measurements on Ta/$Ni_{80}Fe_{20}$/Al_2O_3 trilayer structure. The Kiessing fringes of Ta/$Ni_{80}Fe_{20}$/Al_2O_3 trilayers are more than Al_2O_3/$Ni_{80}Fe_{20}$/Ta stack. The more fringes probably come from the interface effect of SiO_2 and the Ta layer.

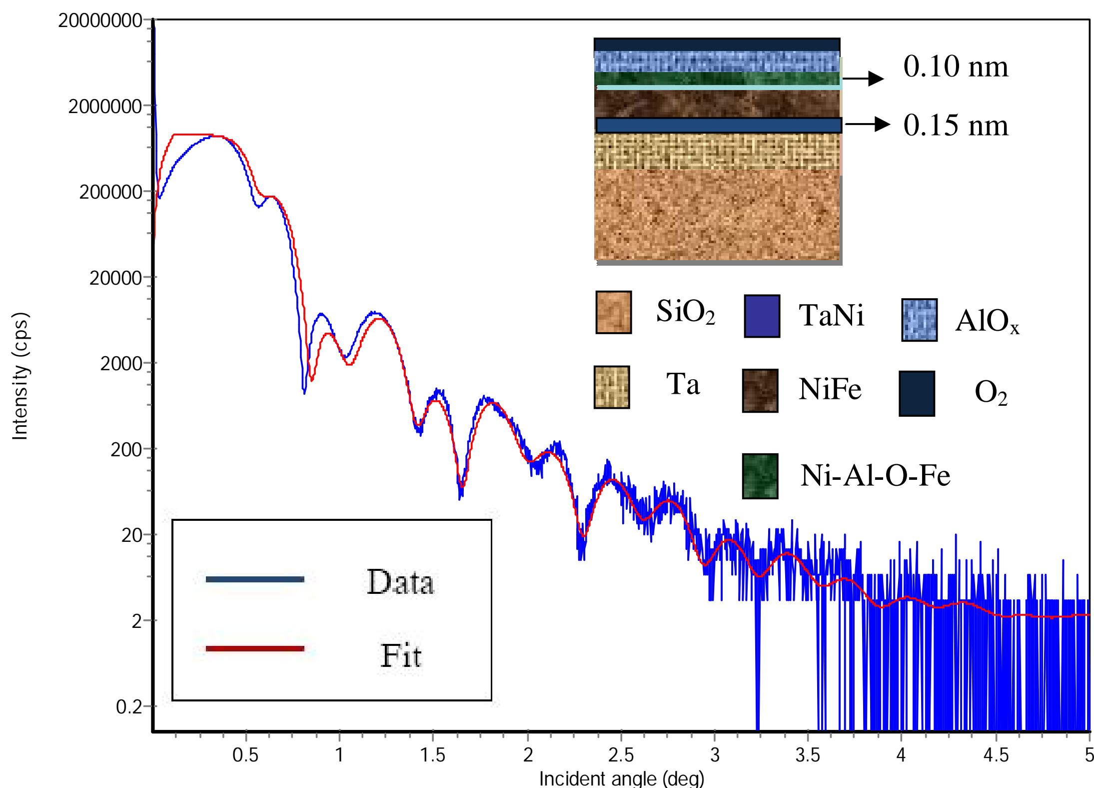

Figure 4.13. XRR measurement of SiO_2/Ta(5 nm)/$Ni_{80}Fe_{20}$(7.6nm)/Al_2O_3(5 nm) layer.

1.5 Å interdiffused layer at the interface of Ta/$Ni_{80}Fe_{20}$ and 1.0 Å layer at the interface of $Ni_{80}Fe_{20}$/Al_2O_3 is measured. Cap Ta_2O_5 creates a interdiffused layer with $Ni_{80}Fe_{20}$ consisting of Al, Ni, Fe and O elements.

Table 4.7. Segmented fit model of SiO_2/Ta(5 nm)/$Ni_{80}Fe_{20}$(7.6 nm)/Al_2O_3(5 nm).

Layer	**Layer Description**	**Density (g/cm3)**	**Thickness(nm)**	**Roughness(nm)**
Substrate	SiO_2	1.114	550000	0.287
1	Ta	20.414	6.078	0.431
2	**Ta 0.50** **Ni 0.50**	8.143	**0.15**	0.213
3	Ni 0.80 Fe 0.20	9.608	7.433	0.420
4	**Al 0.25** **Ni 0.25** **Fe 0.25** **O 0.25**	5.12	**0.10**	0.240
5	Al 0.70 O 0.30	2.948	2.998	0.565
6	O	2.142	2.868	1.35

CHAPTER 5

CONCLUSIONS

Ta/$Ni_{80}Fe_{20}$/Ta, Ta/$Ni_{80}Fe_{20}$/Ta_2O_5, Ta_2O_5/$Ni_{80}Fe_{20}$/Ta_2O_5, Al_2O_3/$Ni_{80}Fe_{20}$/Ta and Ta/$Ni_{80}Fe_{20}$/Al_2O_3 multilayers were grown by magnetron sputtering and magnetic moment of samples were probed by vibrating sample magnetometer (VSM), thickness and roughness of the layers were studied by X ray reflectivity (XRR). Finally, thicknesses of magnetic dead layers were calculated by the help of Liebermann equation.

VSM measurements of the samples yielded that magnetic moment and coercivity of $Ni_{80}Fe_{20}$ alloy is strongly thickness dependent. The superparamagnetic effect is dominated for 1.52 nm of $Ni_{80}Fe_{20}$ ferromagnetic films. Annealing of all trilayer structures decreases the saturated magnetic moment due to distortion of local spin interaction energy in $Ni_{80}Fe_{20}$ lattice. The coercivities of all $Ni_{80}Fe_{20}$ alloys are low and does not change for thicker samples except for 1.52 nm $Ni_{80}Fe_{20}$ films which shows big coercivity is due to non uniform film at the first growth stage.

Magnetic dead layer calculation by the help of Liebermann equation indicates that dead layers are in the order of 1-9 atomic layers. We believe that the MDL forms to a large extend due to interdiffusion at the interface of ferromagnetic and Ta metallic layer. The thickness of MDL is found to be strongly temperature dependent. Annealing decreases the thickness of MDLs for all samples at 300 ˚C except for Ta_2O_5/$Ni_{80}Fe_{20}$/Ta_2O_5 multilayer. 300 ˚C annealing temperature increases the magnetic dead layers of this stack is due to oxygen interdiffusion at the Ta_2O_5/$Ni_{80}Fe_{20}$ interface. At 500 ˚C, interdiffusion at all the interfaces of layers increases and this leads sharp increment of thickness of magnetic dead layers. Comparing to cap Ta metal and Ta_2O_5 insulator, cap Al_2O_3 creates the least MDL thickness that makes Al_2O_3 be best tunneling barrier for TMR based tunnel junction.

X ray reflectivity results confirm that total fitted thicknes of interdiffused layers are very close to the MDL calculated thickness found from magnetization and according to reflectivity fit model Ta is responsible for creating magnetic dead layer which is predicted in the MDL calculation. Further study can be put forward to study the elimination of probability of interdiffused atom near interface of ferromagnetic layer.

REFERENCES

Akhter, M.A., Mapps, D.J., Ma, Y.Q. Thickness and grain-size dependence of the coercivity in permalloy thin films.1997. *Journal of Applied Physics* 81(8): 4122-4124.

Baibich, M.N., J.M. Broto, A. Fert, Van Dau F. Nyugen, F. Petroff, P. Eitenne, G. Creuzet, A. Friederich, and J. Chazelas. 1988. Giant magnetoresistance of (001)Fe/(001)Cr magnetic superlattices. *Physical Review Letters* 61 (21):2472.

Binash, G., P. Grünberg, F. Saurenbach and W. Zinn. 1989. Enhanced Magnetoresistance in layered magnetic structures with antiferromagnetic interlayer exchange. *Physical Review* B 39 (7):4828-4830.

Ding, L., Teng, J., Zhan, Q., Feng, C., Li, M.H., Han, G., Wang, L.J., Yu, G.H., Wang, S.Y. 2009. Enhancement of the magnetic field sensitivity in Al_2O_3 encapsulated NiFe films with anisotropic magnetoresistance. *Applied Physics Letters* (94):162506.

Fert, A., Campbell, I. A. Two-Current Conduction in Nickel. 1968. *Physical Review Letters* 21(16):1190-1192.

Flevaris, N.K. Magneto-optical properties of Pd-Ni multilayer. 1991. *Applied Physics Letters* (58):2177-2179.

Gong, H., Litvinov, D., Klemmer, T.J., Lambeth, D.N., Howard, J.K. 2000. Seed layer effects on the magnetoresistive properties of NiFe films. *IEEE Transactions on Magnetics* 36(5):2963-2965.

Jeong, J.R., Kim, Y.S., and Shin, S.C. 1999. Origins of perpendicular magnetic anisotropy in Ni/Pd multilayer films. *Journal of Applied Physics* 85(8):5762-5764.

Jullière, M. 1975. Tunneling between ferromagnetic films. *Physics Letters* 54A(3):225-226.

Kowalewski, M., W.H.Buttler, N.Moghadam, G.M.Stocks, T.C.Schulthess, K..J.Song, J.R.Thompson, A.S.Arrot, T.Zhu, J.Drewes, R.R.Katti, M.T.McClure, O.Escorcia. 2000. The effect of Ta on the magnetic thickness of permalloy (Ni_{81} Fe_{19}) films. *Journal of Applied Physics* (87):9.

Liebermann, L., J.Clinton, D.M.Edwards, J.Mathon. 1970. Dead layers in ferromagnetic transition layers. *Physical Review Letters* (25):4.

Li, X.L., B.Chen, H.Y.Jing, H.B.Lu, B.R.Zhao and Z.H.Mai, Q. J. Jia. 2005. Experimental evidence of the “deadlayer” at Pt/$BaTiO_3$ interfac. *Applied Physics Letters* (87) :222905.

Long, J.G., Zhai, Y., Chen, J., Du, J., Pan, M.H., Lu, M., Hu, A., Zhai, H.R. 2001. Magnetization property in Ta/NiFe/Ta sandwich structure. *Journal of Magnetism and Magnetic Materials* 226:1823-1824.

Miyazaki, T., N. Tezuka. 1995. Giant magnetic tunneling effect in Fe/Al_2O_3/Fe Junction. *Journal of Magnetism and Magnetic Materials* 139(3):231.

Moodera, J.S., L.R. Kinder, T.M. Wong and R. Meservey. 1995. Largemagnetoresistance at room temprature in ferromagnetic thin film tunnel junctions. *Physical Review Letters* 74(16):3273-3276.

Ohldag, H., A.Scholl, F.Nolting, E.Arenholz, S.Maat, A.T.Young, M.Carey, J.Stöhr. 2003. Correlation between Exchange Bias and Pinned Interfacial Spins *Physical Review Letters* (91):1.

Osgood, R.M., S.K.Sinha, J.W.Freeland, Y.U.Idzerda, S.D.Bader. 1999. X-ray scattering from magnetic, rough surfaces. *Jouırnal of Appied Physics* (85):8.

Parkin, S.S., C. Kaiser, A. Panchula, P.M. Rice, B. Hughes, M. Samant and S.H. Yang. 2004. Giant tunnelling magnetoresistance at room temperature with MgO (100) tunnel barriers. *Nature Materials* 3:862-867.

Qiana, Z., Sivertsen, J.M., Judy, J.H. 1998. Magnetic behavior of NiFe/NiO bilayers *Journal of Applied Physics* 83:6825.

Sattler, K., Siegmann, H.C. 1975. Spin polarized photoelectrons from EuO. *Physical Review B* (20):289-312.

Shinjo, T., Yamamoto, H., Okuyama, T., Araki, S., Mibu, K., Hosoito, N. 1992. Resistivity vs. Magnetic structure in multilayers. *Hyperfine Interactions* (68):1-4.

Si, W., Kurt Williams, Mark Campo, Ming Mao. 2005. Determination and reduction of ion beam etching induced magnetic dead layer. *Journal of Applied Physics* (97):10N901.

Tersoff, J., Falicov, L.M. 1982. Magnetic and electronic properties of Ni films, surfaces, and interfaces *Physical Review B* (26):6186-6200.

Wang, Y.H., Wei-Chuan Chen, Shan-Yi Yang and Kuei-Hung Shen, Chando Park, Ming-Jer Kao and Ming-Jinn Tsai. 2006. Interfacial and annealing effects on magnetic properties of CoFeB thin films. *Journal of Applied Physics* (99):08M307.

Xu, Y.B., E.T.M.Kernohan, D.J.Freeland, A.Ercole, M.Tselepi and J.A.C.Bland. 1998. Evolution of the ferromagnetic phase of ultrathin Fe films grown on GaAs(100)-4x6. *Physical Review B* (2):58.

Yuasa, S., Taro Nagahama, Akio Fukushima, Yoshishige Suzuki and Koji Ando. (2004) Giant room-temperature magnetoresistance in single-crystal Fe/MgO/Fe magnetic tunnel junctions. *Nature Materials* 3:868-871.